

Unsaturated p-Metal Based Metal-Organic Frameworks for Selective Nitrogen Reduction Under Ambient Conditions

Yang Fu¹, Kangkang Li², Munkhbayar Batmunkh³, Hai Yu², Scott Donne¹, Baohua Jia⁴, Tianyi Ma^{1,}*

¹Discipline of Chemistry, School of Environmental and Life Sciences, University of Newcastle, Callaghan, NSW 2308, Australia

²CSIRO Energy, 10 Murray Dwyer Circuit, Mayfield West, NSW 2304, Australia

³Centre for Clean Environment and Energy, Griffith University, Gold Coast, Queensland 4222, Australia

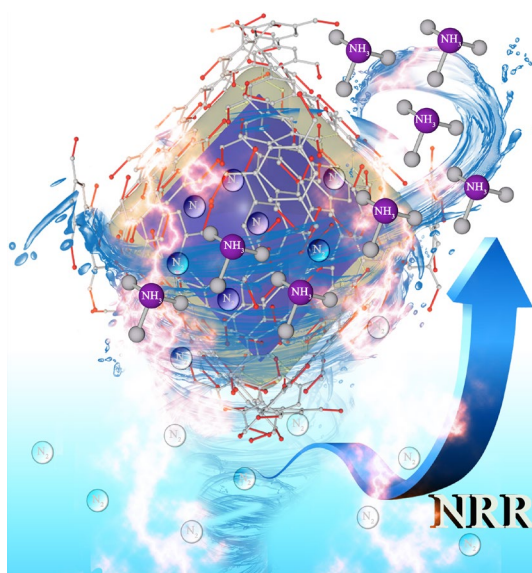
⁴Centre for Translational Atomaterials, Faculty of Science, Engineering and Technology, Swinburne University of Technology, John Street, Hawthorn, VIC 3122, Australia

Corresponding Author

*Email: Tianyi.Ma@newcastle.edu.au

ABSTRACT: Electrochemical ammonia synthesis through the nitrogen reduction reaction (NRR) using renewable electricity has recently attracted significant attention. Of particular importance is the development of efficient electrocatalysts at low costs. Herein, highly selective nitrogen capture using porous aluminum-based metal-organic frameworks (MOFs) materials, MIL-100 (Al), is first designed for the electrochemical NRR in alkaline media under ambient conditions. Owing to the unique structure, MIL-100 (Al) exhibits remarkable electrocatalytic performances (NH_3 yield: $10.6 \mu\text{g h}^{-1} \text{cm}^{-2} \text{mg}_{\text{cat}}^{-1}$, Faradaic efficiency: 22.6%) at a low overpotential (177 mV). Investigation indicates that the catalyst shows excellent N_2 -selective captures due to the unsaturated metal sites binding with N_2 . More specifically, Al as a main-group metal shows a highly selective affinity to N_2 due to the strong interaction between the Al 3p band and N 2p orbitals. The manipulation of multifunctional MOFs delivers both high N_2 selectivity and abundant catalytic sites, leading to remarkable efficiency for NH_3 production.

TOC GRAPHICS



Ammonia (NH_3) is an important chemical for many applications including pharmaceutical, synthetic fibres, and fertilizer production, while also showing great promise for energy storage systems (i.e. hydrogen (H_2) storage).¹⁻⁴ Importantly, it is the only currently known carbon-free energy carrier that does not release carbon dioxide (CO_2). Therefore, it is expected to play a significant role in the future hydrogen economy. However, at present, the traditional energy-intensive Haber–Bosch process is used for ammonia production at high temperature and pressure (300–550 °C and 200–350 atm) with substantial greenhouse gas emission.⁵ There is a growing interest in developing alternative and sustainable approaches for ammonia synthesis. Up to now, environmentally benign processes such as photocatalysis and electrocatalysis without using hydrogen as a reactant through nitrogen reduction reaction (NRR) process under ambient conditions is a rapidly expanding field of research.⁶⁻¹¹

The electrochemical synthesis of ammonia was first discovered in 1807 by Davy et al. who used only water and dissolved air between two gold electrodes.¹² The main challenge for electrochemical method is the slow kinetics of N_2 adsorption and subsequent $\text{N}\equiv\text{N}$ triple bond cleavage. In addition, due to the standard reduction potential for the hydrogen evolution reaction (HER) (0 V vs. Standard Hydrogen Electrode (SHE)) is close to that of NRR (0.057 V vs. Reversible Hydrogen Electrode (RHE)), the competing HER significantly reduces the Faradaic efficiency (FE) of the NRR.⁵ The cell reactors are categorized as either alkaline or acidic systems, but the HER is more dominant in acids as evidenced by the two orders of magnitude higher current density in acidic medium than that in alkaline electrolytes.¹³ In this regard, developing efficient electrochemical NRR catalyst in alkaline media is of great significance.

A key consideration to the design of effective NRR catalysts is the mitigation of the HER. A series of precious metals (e.g., Pt, Au, and Ru) and nonprecious metals (e.g., Fe, Mo, Ni) as electrocatalysts were studied, but the majority of them suffer from poor FEs due to their superior activity for HER over NRR.^{6, 14-18} Recently, researches have confirmed that main

group elements such as Bi, Al, and B are highly active for the NRR due to the strong interaction between *p* band of the main group elements and the N 2p orbitals.¹⁹⁻²¹ For example, Hao et al.¹⁹ reported a strategy in which Bi catalysts and potassium cations both contributed to the electrochemical NRR process with both high selectivity and activity. Their results achieved a record-high FE of 66% and ammonia yield of 200 mmol NH₃ g⁻¹ h⁻¹ in aqueous solution under ambient conditions. In addition, based on thermodynamics studies, their results first suggested main group metals (*p*-block metals) were potentially exhibiting much higher electrochemical NRR selectivity and activity than the intensively studied transition metals (*d*-block metals) due to the stronger interactions between the *p* orbitals of metal substrates and the adsorbed nitrogen. Further, based on this strategy, our previous study revealed for the first time the behavior of molybdenum aluminum boride (MoAlB) single crystals as a new family of NRR catalysts based on the transition metal aluminum borides (MAB phase).²¹ The mechanism studies also indicated that the B and Al as main-group elements showed a highly selective affinity to the N₂ due to the robust coupling of B 2p and Al 3p bands towards the N 2p orbital, which resulted in excellent NRR and largely suppressing the competitive HER. Thus, in comparison to transition metal-based catalysts, the main group element-based catalysts are promising in that they provide abundant opportunities to develop effective NRR catalysts while mitigating the competing HER.

On the other hand, for the NRR process via an electrochemical approach, the energy input to boost chemical kinetics can be reduced efficiently by virtue of favorable heterogeneous electrocatalysts.²² Compared to homogeneous catalysts, heterogeneous catalysts possess many advantages, such as better stability for long-term use in aqueous electrolyte and better incorporation capability into electrodes, resulting in improved energy conversion efficiencies.^{23, 24} Owing to high microporosity, large surface area, and a tunable structure, metal–organic frameworks (MOFs), as an emerging class of highly ordered porous coordination polymer consisting of metal centers and organic linkers, are regarded as

promising materials in a large variety of applications,²⁵⁻²⁹ particularly in gas adsorption, capture, and separation, and heterogeneous catalysis.³⁰⁻³³ The presence of the microporous structure in solvents is essential for gas-phase catalysis as well as for gas or small molecule storage and separation,²⁷ which is an important requisite for good catalysts. Moreover, the highly ordered MOFs are characterised by the high density of individually coordinated metal atoms (or clusters) with organic ligands and contain well-defined and regularly isolated active sites facilitating their sufficient exposure to reactions intermediates. As such they are favourable for good electrocatalytic performance³⁴ and promising as efficient catalysts for the NRR. For example, Wu et al.⁵ used a MOF-derived nitrogen-doped nanoporous carbon as an electrocatalyst for the NRR and Luo et al.³⁵ developed MOF-derived nitrogen-doped carbon/Co₃O₄ nanocomposites with core-shell structures as an efficient nitrogen fixation electrocatalyst, demonstrating the highest performance with NH₃ yield rate of 3.4 $\mu\text{mol cm}^{-2} \text{h}^{-1}$ and 42.58 $\mu\text{g h}^{-1} \text{mg}_{\text{cat.}}^{-1}$ and FE of 10.2% and 8.5%. However, the FE is low. In addition, previous research have reported designing porous MOFs containing unsaturated metal sites to strongly bind N₂ provides a promising route to achieving N₂-selective capture.³⁶⁻³⁸ Inspired by this concept, Yoon et al.³⁹ reported mesoporous MOF materials containing accessible Cr(III) sites (MIL-100) able to selectively capture N₂. Further, Cui et al.²² employed density functional theory (DFT) calculations to understand N₂ and H₂O adsorption on a series of 2D MOFs, presenting a great capability for N₂ activation due to a much stronger adsorption with nitrogen than H₂O. It also provides atomic level insights that the MOFs with abundant metal sites can show strong affinity to N₂ molecules. These work open up a new research avenue for the development of NRR by providing an adsorption-based technologies and has inspired further studies on use of MOFs for efficient NH₃ synthesis.

Herein, we report for the first time the use of aluminum-based porous MOF (MIL-100 (Al)) to selectively reduce N₂during electrochemical ammonia synthesis in alkaline electrolytes under ambient conditions. Thanks to the strong interactions between active sites and nitrogen

atoms within the specific framework structure, the MIL-100 (Al) supported on a free-standing copper foam (Cu foam) exhibits a high electrocatalytic NRR activity and selectivity at a low overpotential in a 0.1 M KOH electrolyte under ambient conditions. The catalysts can be prepared at low cost due to the high abundance and low price of the starting Al materials. Considering the low cost and high performance, the MOF materials designed in this work can be promising catalysts for large scale production of ammonia using electrochemical NRR processes.

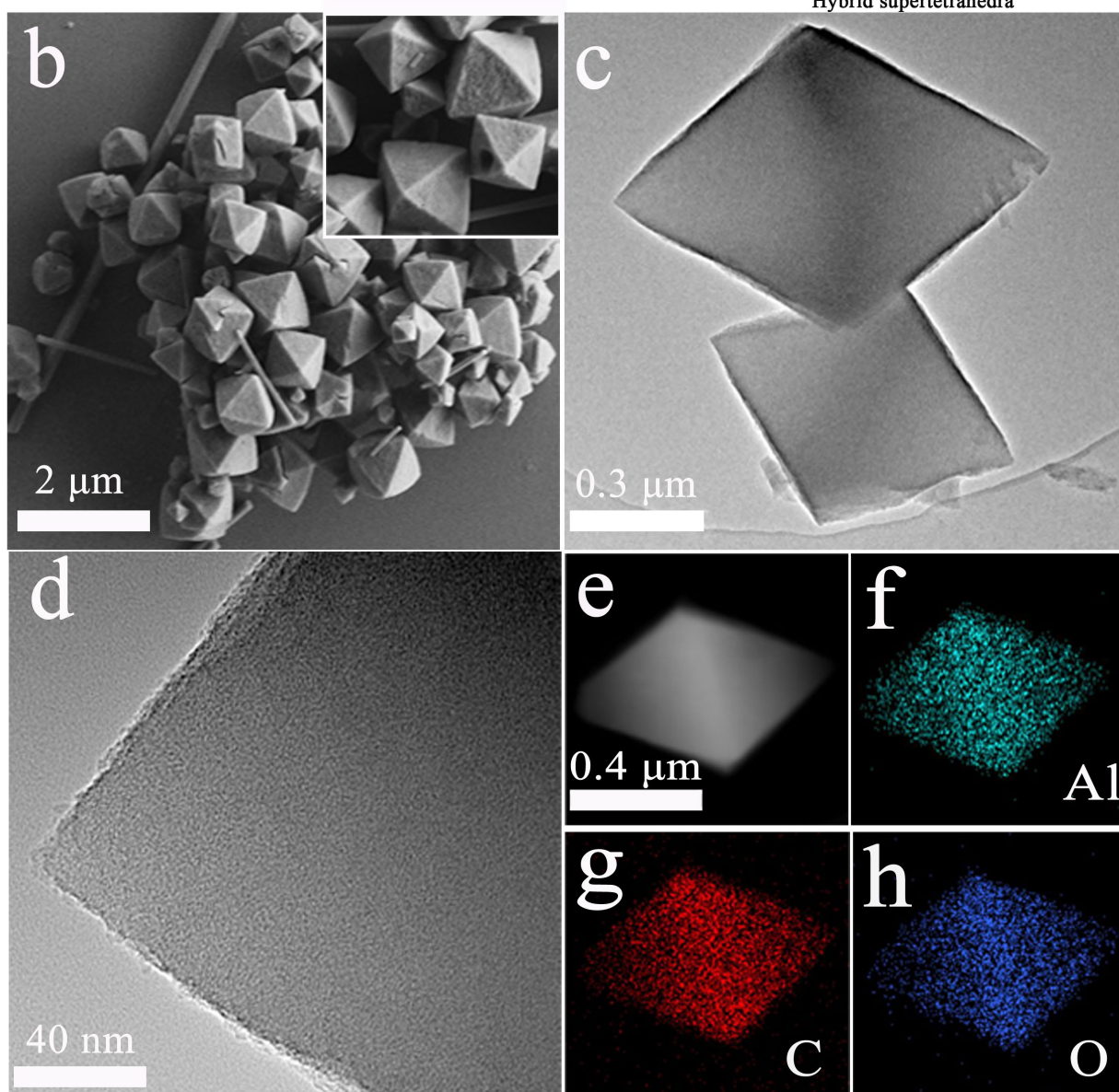
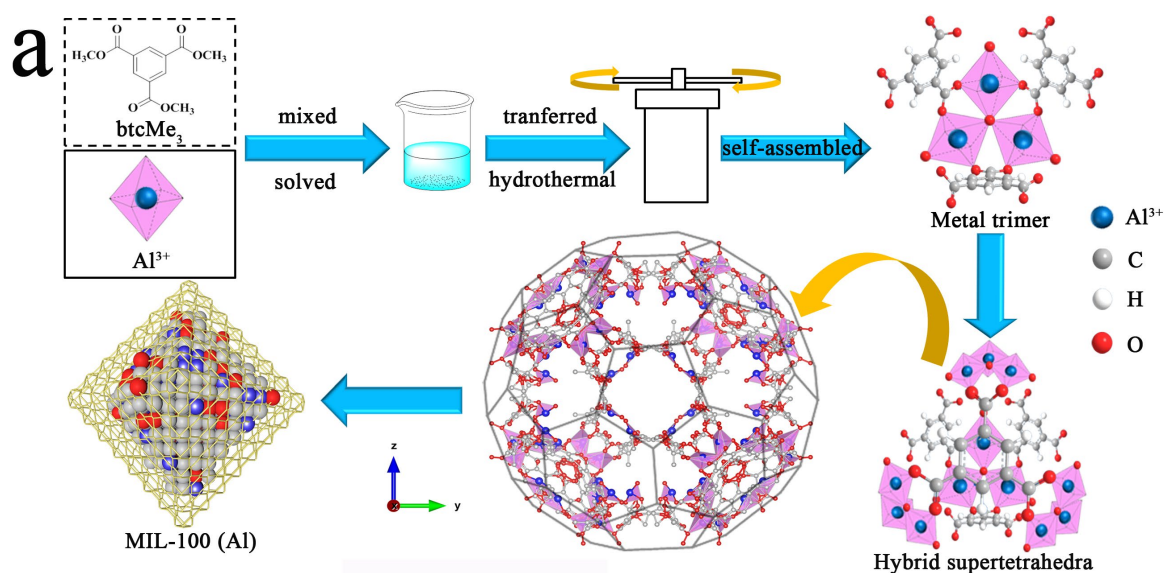


Figure 1a. Illustration of the synthesis process for the preparation of MIL-100 (Al). **b.** SEM image, **c.** TEM image, **d.** HRTEM image, **e-h.** HAADF-STEM image and the corresponding EDS elemental mapping of the MIL-100 (Al).

The synthetic procedure of our MIL-100 (Al) is schematically illustrated in Figure 1a and is described in detail in supporting information. In this work, the nano-/micro-structure of the as-prepared MIL-100 (Al) was first examined using a scanning electron microscopy (SEM). As shown in Figure 1b, the MIL-100 (Al) shows a highly uniform monodisperse octahedron with an average size of around 1 μm . Transmission electron microscopy (TEM) image displayed in Figure 1c also indicates an apparent octahedral-shape feature, which is consistent with the SEM analysis. A plenty of porous structures on the surface of the MIL-100 (Al) were clearly observed in a high-resolution TEM (HRTEM) image (Figure 1d), which is due to the framework structure from metal centers and organic linkers. High-angle annular dark field-scanning transmission electron microscopy (HAADF-STEM) image and corresponding Energy-dispersive X-ray spectroscopy (EDS) elemental mapping images of the MIL-100 (Al), displayed in Figure 1e-h, further verified the homogeneous distribution of Al, C and O in the sample. No other phases were observed in the SEM and TEM images, indicating that the single phase product was successfully obtained.

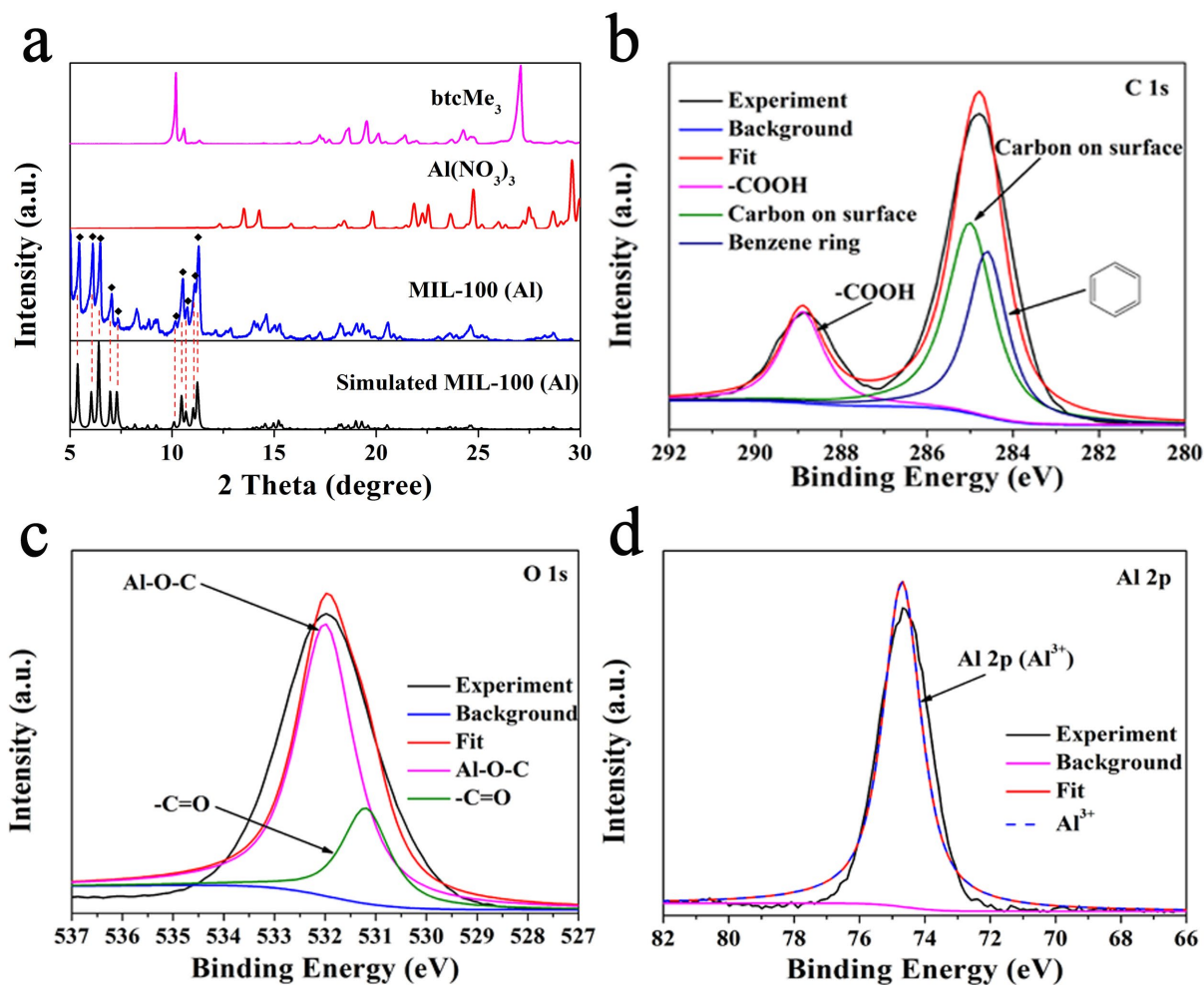


Figure 2a. XRD patterns of btcMe_3 , $\text{Al}(\text{NO}_3)_3$, and MIL-100 (Al). XPS spectra of **b.** C 1s, **c.** O 1s, **d.** Al 2p of the MIL-100 (Al).

X-ray diffraction (XRD) was utilized to confirm the structure and composition of btcMe_3 , $\text{Al}(\text{NO}_3)_3$ and MIL-100 (Al) samples. As shown in Figure 2a, according to the reference and stand simulated XRD patterns derived by cif. data of MIL-100 (Al),⁴⁰ the feature of a pure MIL-100 phase shows five peaks located within the 2θ angle range from 5 to 7.5 degree and another five peaks within the 2θ angle range from 10 to 12.5 degree, which reveals a collection of single crystalline phase ground into a powder matching well with the simulated one reported in the literature.⁴⁰ Compared to the diffraction peaks of the other two samples, these peaks were not observed, indicating that the MIL-100 (Al) is successfully prepared. In addition, based on the crystal structure analysis (Figure S1), the stand simulated XRD patterns of the MIL-100 (Al) have similar peaks with that of the MIL-100 (Fe),^{40, 41} indicating that the

MIL-100 (Al) structures have identical topologies with MIL-100 (Fe), built from trimers of metal octahedrons and organic benzene-1,3,5-tricarboxylate (BTC) linkers. Thus, the detailed mechanism of the formation of MIL-100 (Al) is shown in Figure 1a. First, these metal trimers connect with the BTC molecules to form a hybrid supertetrahedron unit. Four vertices of the hybrid supertetrahedron are occupied by the trimers while the organic linkers are located at the four faces of the hybrid supertetrahedron. Finally, the supertetrahedra further assemble into a 3D space architecture. The architecture has the characteristics of an octahedral morphology and symmetric crystallographic structure.⁴²

XPS as a versatile analysis technique was used to analyze the composition and chemical state of MOFs. Figure S2 shows the XPS spectrum of MIL-100 (Al) with three peaks appearing at 74.0, 285.0, and 531.5 eV which correspond to the Al 2p, C 1s, and O 1s, respectively. The elemental composition confirmed by XPS spectra is consistent with the EDS results in Figure S2 and Table 1. The XPS spectrum of C 1s is shown in Figure 2b and can be deconvoluted into three peaks centered at 284.8, 285.1 and 288.9 eV. The peaks at 284.8 and 288.9 eV can be assigned to phenyl and carboxyl signals, respectively. The peak at about 285.1 eV is assigned to the carbon on the sample surface. It may be attributed to conductive adhesive from the substrate.⁴³ The O 1s peak at 531.5 eV shown in Figure 2c can be deconvoluted into two peaks located at 531.2 and 532.0 eV, which can be attributed to the carboxide and Al-O-C species, respectively.⁴⁴ Figure 2d provides a high resolution XPS spectrum of the Al 2p signal deconvoluted into one peak located at 74.5 eV, which is assigned to the Al-O-C.⁴⁵ These results strongly indicate that the MIL-100 (Al) was synthesized successfully.

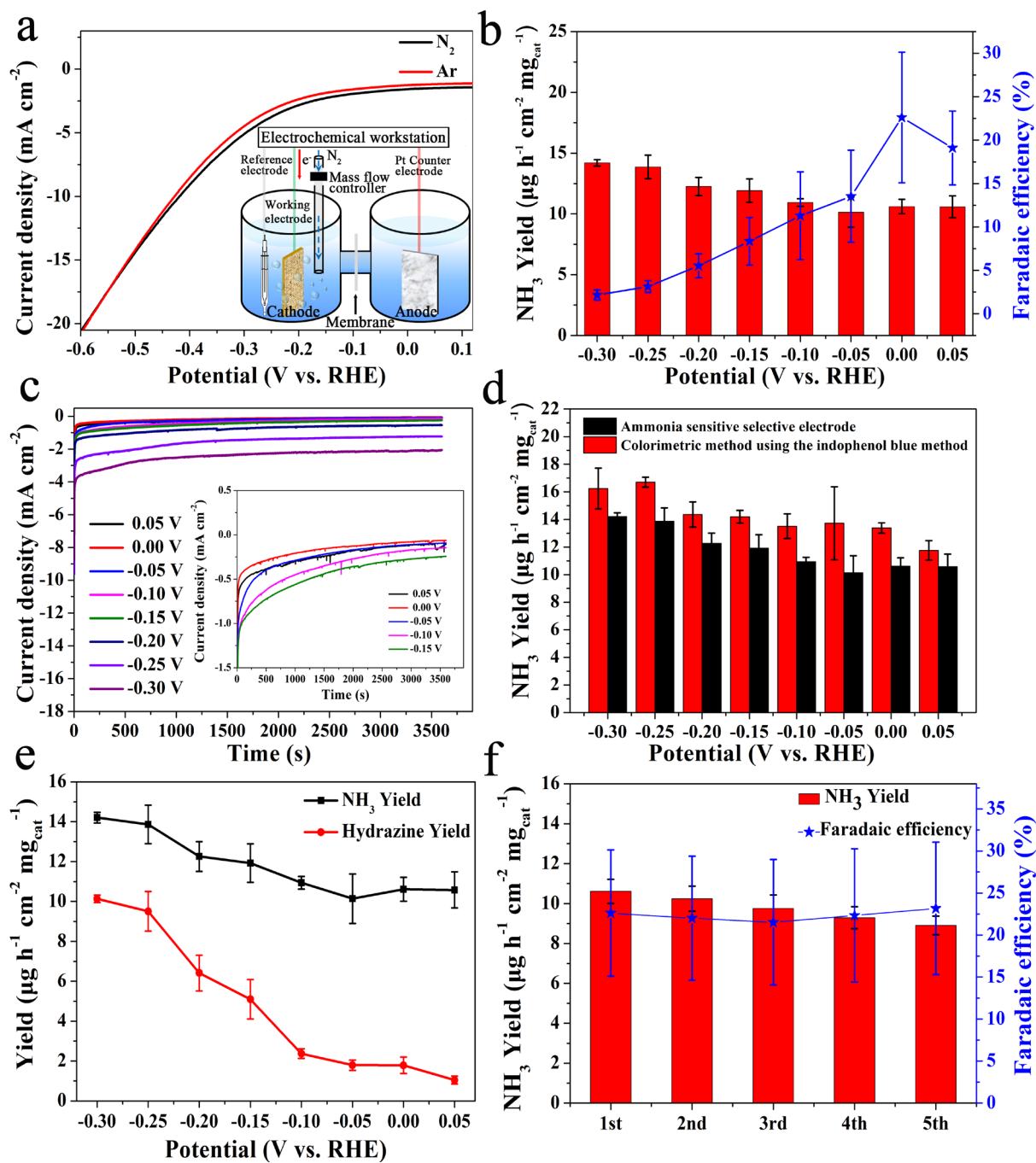


Figure 3a. LSV curves of MIL-100 (Al) /Cu foam electrode in N_2 and Ar-saturated aqueous solutions of 0.1 M KOH with inset showing the schematic diagram of electrochemical NRR setup. **b.** Faradaic efficiency and ammonia yield at different potentials ranging from 0.05 to -0.30 V vs. RHE for MIL-100 (Al). **c.** Chronoamperometry results at the corresponding potentials. **d.** Comparison of the ammonia sensitive selecting electrode and Indophenol blue reagent based colorimetric method for the quantitative analysis of ammonia yield. **e.** Indophenol blue reagent based colorimetric method for the quantitative analysis of ammonia yield and Watt & Chrisp method for the quantitative analysis of hydrazine yield. **f.** Faradaic efficiency and ammonia yield during 5 consecutive cycles.

To evaluate the electrocatalytic NRR activities of our MIL-100 (Al), electrochemical tests were performed in a N₂-saturated 0.1 M KOH electrolyte under ambient conditions. Electrochemical linear sweep voltammetry (LSV), chronoamperometry and electrochemical impedance spectroscopy (EIS) were scanned at different applied potentials. All tests were performed in a two-compartment cell separated by a proton conductive cation exchange membrane (Nafion® 117), in which the protons (H⁺) can react with N₂ to form ammonia over the catalyst. At first, the LSV curves for MIL-100 (Al) in Ar and N₂-saturated 0.1 M KOH solutions were measured to verify the source of ammonia (Figure 3a). In the Ar-saturated solution, the increase in current density after -0.1 V vs. RHE was caused by the HER, which competed with the NRR. In contrast, when the applied potential was more positive than -0.5 V vs. RHE, a clear reduction in the current density for the N₂-saturated solution was observed as compared to that of the Ar-saturated solution. This provides evidence that the catalytic reduction of N₂ to NH₃ does in fact take place in this system. When the applied potential was set more negative than -0.5 V vs. RHE, the current densities in N₂-saturated and Ar-saturated solutions were very close, due to the dominant behavior of HER compared to the NRR at relatively higher overpotential. In addition, for further confirmation of successful ammonia synthesis, the corresponding NH₃ concentrations were measured by using the ammonia-selective electrode method for qualitative analysis of ammonia in the electrolyte after 1 h of electrolysis in a continuous Ar and N₂ bubbling (further details are provided in the SI, Figure S4). This test clearly shows that the values of NH₃ yield are derived from the NH₃ concentrations. In the Ar system, negligible ammonia was detected in the electrolyte due to background signal interference. These results demonstrate that the N sources for ammonia synthesis is exclusively provided by the N₂ feed gas, indicating that the electrocatalytic N₂ reduction can be realized by the as-prepared MIL-100 (Al).

Figure 3b shows the Faradaic efficiencies (FEs) and ammonia yields of our MIL-100 (Al) at various applied potentials ranging from 0.05 to -0.30 V vs. RHE. The FE and NH₃ yields

shown in Figure 3b are measured based on the ammonia-selective electrode method. As shown in Figure 3b, ammonia yields at various applied potentials show an increasing trend with increasing the applied potential. However, a gradual decreasing trend in the FEs was observed as the applied potential is shifted from 0.05 to -0.30 V vs. RHE, except for the applied potential of 0 V vs. RHE (equal to overpotential of 177 mV, defined as the difference between equilibrium potential and applied potential). In fact, as depicted in Figure 3c, a remarkable increase in the current density was observed with the increase of applied potential. A possible explanation is the fact that due to more electrons produced at higher applied potentials, more electrons take part in the NRR process, thus resulting in improved conversion of N_2 to NH_3 . In other word, increasing overpotentials is favorable for the protonation process during NH_3 generation. However, the HER became more dominant with an increase of overpotentials due to the high affinity of the MIL-100 (Al) surface for H-adatoms, suppressing the production of NH_3 and resulting in the decline of the FEs for NH_3 .^{20, 46, 47} The competing HER and NRR led to the the highest NH_3 FEs being achieved at the optimum overpotential (177 mV). Therefore, in all comparative experiments, the overpotential was determined to be the most appropriate. The NH_3 yield (normalized based on the weight of the catalysts) and FEs of the MIL-100 (Al) at a low overpotential were $10.6 \mu\text{g h}^{-1} \text{cm}^{-2} \text{mg}_{\text{cat}}^{-1}$ and 22.6%, respectively (Figure 3b). To our knowledge, NRR catalysts with low overpotential and high NH_3 selectivity have been rarely reported, especially MOFs. For instance, Xin et al.⁴⁸ reported single Mo atoms anchored to nitrogen-doped porous carbon as a cost-effective catalyst for the NRR, achieving a high NH_3 yield rate ($34.0 \text{ mg NH}_3 \text{ h}^{-1} \text{mg}_{\text{cat}}^{-1}$) and a promising FE (14.6%) at -0.3 V vs. RHE. Besides, Luo et al.⁴⁹ synthesized MOF-derived C@NiO@Ni microtubes performing well in NRR, reaching both a high NH_3 yield rate of $43.15 \mu\text{g h}^{-1} \text{mg}_{\text{cat}}^{-1}$ and a FE of 10.9% at -0.7 V vs. RHE. We compared our values with previously reported literatures (Table S3). Our MIL-100 (Al) achieved remarkable NH_3 yields and FEs at a low applied potential. Therefore, an ultralow overpotential (177 mV), which is

close to the theory equilibrium potential, is used for MIL-100 (Al), making it one of the most active and selective electrocatalysts for future NRR research under ambient conditions.

In addition, to confirm the reliability of the ammonia-selective electrode method for ammonia detection, we also used an indophenol blue reagent (Figure 3d). It was found that the NH_3 yield values determined by the colorimetric method are slightly higher than those measured by the ammonia-selective electrode method possibly due to potential contaminants (metal residues, etc.), which have been found in literature.^{50, 51} Furthermore, it has been reported that the determination of ammonia-selective electrode is not interfered by the contaminants. Since hydrazine (N_2H_4) is a possible by-product during the electrocatalytic NRR, the colorimetric method was also used to determine if any N_2H_4 was produced. Differing from most of previous reports, both NH_3 and hydrazine hydrate ($\text{N}_2\text{H}_4 \cdot \text{H}_2\text{O}$) were detected in the electrolyte after 1 h of electrolysis in a continuous N_2 bubbling, and the average yields and corresponding Faradaic efficiencies under various electrode potentials are listed in Figure 3e and Table S2 (Supporting Information), indicating that the as-prepared MIL-100 (Al) electrode still has a good selectivity for the NRR.

The stability of our MIL-100 (Al) for the electrocatalytic N_2 reduction was evaluated by consecutive cycling electrolysis at the overpotential (177 mV). The ammonia yields and FEs show no significant changes during 5 consecutive cycles (Figure 3f), indicating the high stability of MIL-100 (Al) for electrochemical N_2 reduction. Additionally, the stability of the MIL-100 (Al) was also assessed by scanning at a constant overpotential of 177 mV for 10 h. The current density presents no obvious changes (Figure S5), further indicating that the MIL-100 (Al) can effectively produce NH_3 over a long period of time. Therefore, these results confirm that this MOF structure has an excellent chemical stability during the NRR process.

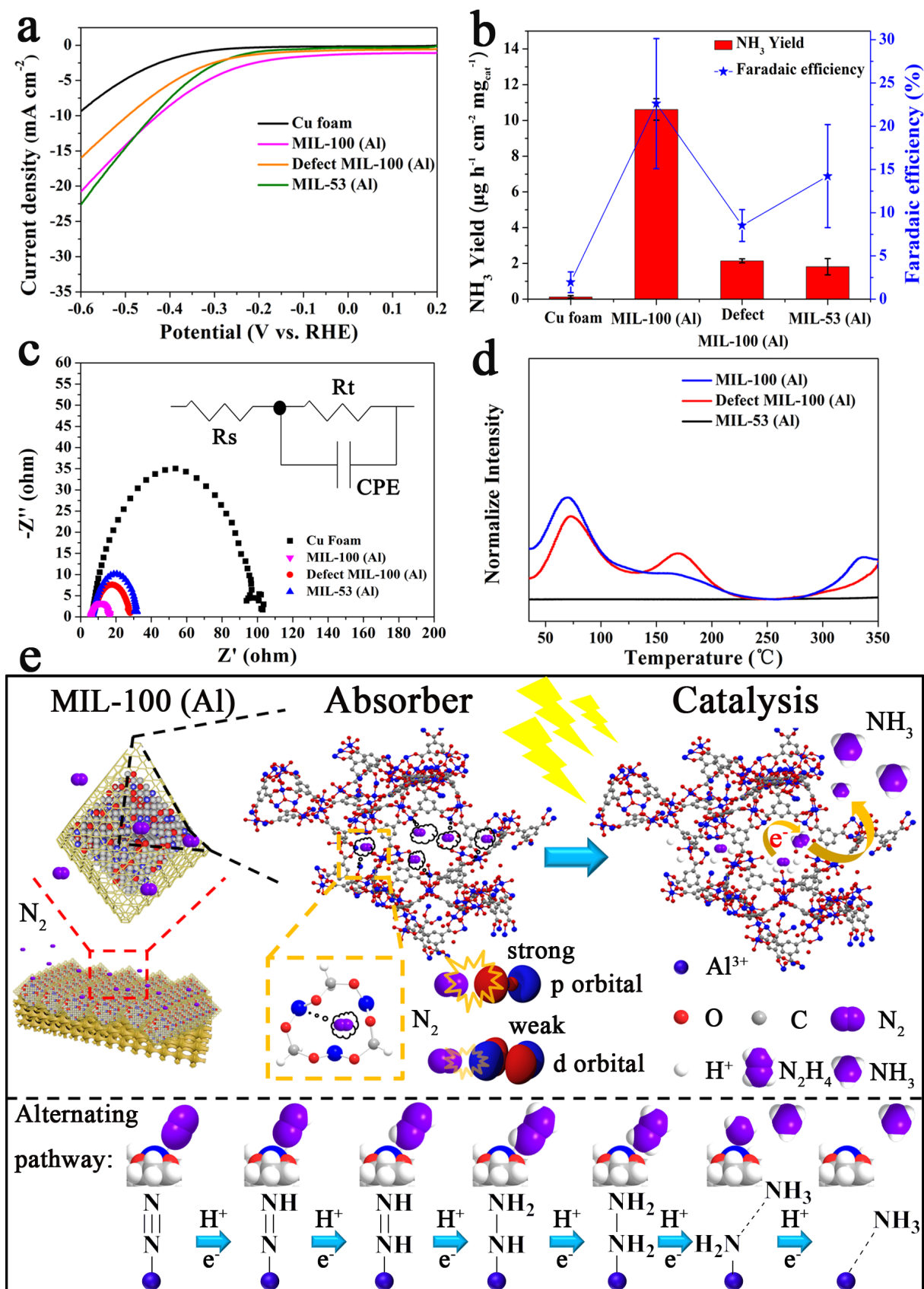


Figure 4a. LSV curves of pure Cu foam, MIL-100 (Al), defect MIL-100 (Al) and MIL-53 (Al) electrodes in an N_2 -saturated aqueous solution of 0.1 M KOH. **b.** Comparison of Ammonia yield and Faradaic efficiencies at the overpotential (177 mV) for pure Cu foam, MIL-100 (Al), defect MIL-100 (Al), and MIL-53 (Al) electrodes in an N_2 -saturated aqueous solution of 0.1 M KOH. **c.** EIS (recorded at -0.3 V vs RHE with inset showing the

equivalent circuit diagram) of pure Cu foam, MIL-100 (Al), defect MIL-100 (Al), and MIL-53 (Al) in an N₂-saturated aqueous solution of 0.1 M KOH. **d.** The N₂-TPD of MIL-100 (Al), defect MIL-100 (Al), and MIL-53 (Al). **e** Mechanism of electrochemical NRR based on MIL-100 (Al).

To evaluate the electrocatalytic NRR mechanism of MIL-100 (Al) under ambient conditions, a series of comparison tests were performed. Firstly, to investigate the impact of the specific MOFs structure for NRR, MIL-53 (Al) catalysts, different from MIL-100 (Al), were synthesized. According to the reference,⁵² the experimental XRD pattern and morphology of the synthesized MIL-53 (Al) (Figures S6 and S7) is in good agreement with the one reported in the literature, showing the successful preparation of MIL-53(Al). In Figure 4a and 4b, as compared to MIL-100 (Al)/Cu foam, pure Cu foam and MIL-53 (Al)/Cu foam specimens exhibit lower reduction current density and almost no ammonia detection at the same applied potential. This confirms that they possess no electrocatalytic activity towards the NRR process, which indicates that the specific structure most likely plays a critical role in achieving the benefit of better selective N₂ binding and catalytic role in the electrochemical NRR process. Previous reports¹⁸⁻²⁰ have verified that the main group metals (*p* metals) can exhibit much higher electrochemical NRR selectivity and activity than the intensively studied transition metals (*d* metals) due to the stronger interactions between the *p* orbitals of the metal substrates and nitrogen. To the best of our knowledge, most metals with a theoretically high electrocatalytic NRR activity are transition metals, but they exhibit a very poor selectivity due to the strong HER competition. To confirm the importance of aluminum as a main-group metal in the process of NRR, the NRR tests of Al/Cu foam and Mo/Cu foam were compared. Figure S8 demonstrates the NH₃ yield and FEs of Al are much higher than those of Mo. It is conceived that the MIL-100 catalysts containing aluminum, have a high affinity for N-adatoms which helps suppress the production of hydrogen and leads to a higher NRR selectivity at these potential. Additionally, it also confirms unsaturated metal sites as a lewis acid exposed in the MOF structure can withdraw *p* electrons from N₂ molecules and weaken

the $\text{N}\equiv\text{N}$ bonds (Figure S8). Recently, it has unequivocally demonstrated that missing cluster defects can be obtained when synthesized in the presence of excessive monocarboxylic acid modulators under the most commonly employed conditions.⁵³ Thus, to further evaluate the influences of Al on the structure of MIL-100 and NRR process, a preliminary investigation into the defect chemistry of MIL-100 (Al) was presented in this paper. As shown in thermogravimetric analysis (TGA) presented in Figure S9, defect-rich MOFs had lower thermal stabilities in comparison to their “non-defective” analogues.⁵⁴ This is due to the solvated water filling up such vacancies.⁵⁵ Powder X-ray diffraction (XRD) patterns of defective derivatives (Figure S10) display similar lattice information as the patterns of the respective parent frameworks, confirming that they retain the long-range order and topology of the parent framework.⁵⁶ However, due to the presence of randomly located defects, the losses in short-range order lead to the weakening intensity and shift of peaks. It can be seen that most of the patterns contain a broad and strong peak spanning at 2θ range of ca. $5\text{-}12^\circ$. This peak cannot be attributed to the MIL-100 phase and could be “missing cluster defects”.⁵³ Compared to the MIL-100 (Al), the defect MIL-100 (Al) exhibits lower NH_3 yield and FEs (Figure 4b) It was assumed that the missing cluster defects could result in some Al lack of MIL-100 structure, decreasing NRR active sites and thus negatively affecting ammonia production.

Additionally, we provide further discussion based on the EIS measurements (Figure 4c and S11). The electron transfer resistance (R_t) at the electrode surface is derived from the semicircle domains of impedance spectra, which is used to describe the interface properties of the electrode. The semicircle diameter of MIL-100 (Al) is much larger than that of the control group of catalysts (Mo). However, diameters for the Al, defect MIL-100 (Al), MIL-53 (Al), and pure Cu foam are much bigger than that of the MIL-100 (Al). On the one hand, this is due to the lower contact and charge transfer impedance in the MIL-100 (Al) consisting of Al and O. On the other hand, the poor reactivity shown by Al, defect MIL-100 (Al), MIL-53 (Al),

and pure Cu foam indicates that less charge transfer is involved in the reaction, which is consistent with the data presented in Figures 4a and S12. In the previous work,^{18, 20} owing to the strong binding with nitrogen and the slow of certain intermediates, the NRR activity could be limited. Due to the critical step of N₂ adsorption for the NRR process, the N₂ adsorption behaviors of MIL-100 (Al) were further evaluated by temperature-programmed desorption of N₂ (N₂-TPD) in Figure 4d. In general, two adsorbed N₂ peaks could be observed. The peak at low temperature range is related to the physical adsorption while the peak observed at high temperature ranges is related to the chemisorption species of N₂. This result indicates that N₂ can be chemically and physically adsorbed on the MIL-100 (Al) and defect MIL-100 (Al). In contrast, there is almost no N₂ adsorption on the MIL-100 (53). Therefore, the strong N₂ adsorption ability of the porous MIL-100 structure is favorable for enhancing NH₃ production kinetics. According to the peak area, N₂ adsorption on the MIL-100 (Al) is stronger than that on the defect MIL-100 (Al), suggesting that MIL-100 (Al) exhibits a higher N₂ adsorption capacity due to different porous sizes. Besides, Al metal atoms also contribute to the N₂ adsorption because the nitrogen vacancies could introduce many adsorption sites on the surface of the catalysts. As chemisorption is generally associated with the activation, these adsorption sites can activate N₂ for nitrogen fixation.⁵⁷ Thus, the higher nitrogen vacancy concentration of MIL-100 (Al) results in more chemical adsorption sites, leading to the higher NRR performance. Moreover, other researches have confirmed that the chemisorption process in this structure occurs on the metal surfaces.^{21, 39, 58} Therefore, we propose that the unsaturated Al with the unique MOF structure in MIL-100 (Al) should play a synergistic role in facilitating the electrocatalytic NRR process.

A study by Yoon et al.³⁹ has confirmed that the hydrothermally stable series of mesoporous metal(III) trimesates MIL-100(M) containing a large concentration of chemically tunable unsaturated metal sites (Al, Cr or Fe) offers a unique opportunity to validate our proposed concept. This family of porous solids built up from oxo-centred trimers of metal(III)

octahedra interconnected by 1,3,5-benzene tricarboxylate (BTC) linkers shows a zeotype architecture with two types of mesoporous cages, accessible through microporous windows. Once activated, two of the three metal (III) sites are unsaturated, and -OH group caps the third metal ion.³⁴ Meanwhile, Therefore, MIL-100 with a large internal surface area/pore volume can be explored as potential adsorbents for selective N₂ separation/capture. Furthermore, based on the fact that NH₃ and N₂H₄ were also detected experimentally, the proposed alternate pathway pathways representative of NH₃ and N₂H₄ production are further demonstrated in Figure 4e. On the basis of the above discussion, the mechanism of electrochemical NRR based on MIL-100 (Al) is also described in Figure 4e. Firstly, N₂ is adsorbed and further accumulated on the surface of the MIL-100 (Al) by strong binding between N and Al. Subsequently, with H⁺ absorbing and binding with N on the surface of MIL-100 (Al), Al acting as a catalytic site reduces N₂ to NH₃ gradually.

In summary, MIL-100 (Al) MOF materials are designed as new candidate electrocatalysts for electrochemical ammonia synthesis under ambient conditons. They have demonstrated a high level of activity towards the electrochemical NRR in alkaline electrolytes. The as-synthesized MIL-100 (Al) afforded an NH₃ yield of 10.6 $\mu\text{g h}^{-1} \text{cm}^{-2} \text{mg}_{\text{cat.}}^{-1}$ and a FE of 22.6% at a low overpotential (117 mV). Mechanistic studies show that the outstanding NRR activity of MIL-100 (Al) is attributed to the synergistic role of Al with the specific framework structure. Due to their strong N₂ capture and ability to overcome the competing HER at reactive sites, the MIL-100 (Al) possess high NRR activity and selectivity. Excellent catalytic performance and long-term stability of MIL-100 (Al), suggests that this system has a promising potential in the electrocatalytic NRR processes.

ASSOCIATED CONTENT

Supporting Information

The Supporting Information is available free of charge at [Experimental Section](#) and additional supplementary figures and tables about material and device characterization.

AUTHOR INFORMATION

Corresponding Author

Tianyi Ma — Discipline of Chemistry, School of Environmental and Life Sciences, University of Newcastle, Callaghan, NSW 2308, Australia; Email: Tianyi.Ma@newcastle.edu.au

Notes

The authors declare no competing financial interest.

ACKNOWLEDGMENT

This work was financially supported by China Scholarship Council (Grant 201804910553; Y. F.), Australian Research Council (ARC) through Discovery Early Career Researcher Award (DE150101306) and Linkage Project (LP160100927), Faculty of Science Strategic Investment Funding of University of Newcastle, and CSIRO Energy Top-up Scholarship.

REFERENCES

- (1) Appl M., Ammonia Principles and Industrial Practice. *WileyVCH*, New York **2007**, 1–310.
- (2) Coric I.; Mercado B.-Q.; Bill E.; Vinyard D.-J.; Holland P.-L. Binding of Dinitrogen to an Iron–Sulfur–Carbon Site. *Nature* **2015**, 526, 96–99.
- (3) Spatzal T.; Perez K.-A.; Einsle O.; Howard J.-B.; Rees D.-C. Ligand Binding to the FeMo-Cofactor: Structures of CO-Bound and Reactivated Nitrogenase. *Science* **2014**, 345, 1620–1623.
- (4) Chen G.-F.; Ren S.-Y.; Zhang L.-L.; Cheng H.; Luo Y.-R.; Zhu K.-H.; Ding L.-X.; Wang H.-H. Advances in Electrocatalytic N₂ Reduction—Strategies to Tackle the Selectivity Challenge. *Small Methods* **2019**, 3, 1800337.
- (5) Mukherjee S.; Cullen D.-A.; Karakalos S.; Liu K.-X.; Zhang H.; Zhao S.; Xu H.; More K.-L.; Wang G.-F.; Wu G. Metal-Organic Framework-Derived Nitrogen-Doped Highly Disordered Carbon for Electrochemical Ammonia Synthesis using N₂ and H₂O in Alkaline Electrolytes. *Nano Energy* **2018**, 48, 217–226.
- (6) Li S.-J.; Bao D.; Shi M.-M.; Wulan B.-R.; Yan J.-M.; Jiang Q. Amorphizing of Au Nanoparticles by CeO_x–RGO Hybrid Support towards Highly Efficient Electrocatalyst for N₂ Reduction under Ambient Conditions. *Adv. Mater.* **2017**, 29, 1700001.
- (7) Chen G.-F.; Cao X.; Wu S.; Zeng X.; Ding L.-X.; Zhu M.; Wang H. Ammonia Electrosynthesis with High Selectivity Under Ambient Conditions via a Li⁺ Incorporation Strategy. *J. Am. Chem. Soc.* **2017**, 139, 9771–9774.
- (8) Chen S.; Perathoner S.; Ampelli C.; Mebrahtu C.; Su D.; Centi G. Electrocatalytic Synthesis of Ammonia at Room Temperature and Atmospheric Pressure from Water and

Nitrogen on a CarbonNanotube-Based Electrocatalyst. *Angew. Chem. Int. Ed.* **2017**, *129*, 2743–2747.

(9) Chen S.; Perathoner S.; Ampelli C.; Mebrahtu C.; Su D.; Centi G. Room-Temperature Electrocatalytic Synthesis of NH_3 from H_2O and N_2 in a Gas–Liquid–Solid Three-Phase Reactor. *ACS Sustain. Chem. Eng.* **2017**, *5*, 7393–7400.

(10) Duman L.-M.; Farrell W.-S.; Zavalij P.-Y.; Sita L.-R. Steric Switching from Photochemical to Thermal Reaction Pathways for Enhanced Efficiency in Metal-Mediated Nitrogen Fixation. *J. Am. Chem. Soc.* **2016**, *138*, 14856–14859.

(11) Bat-Erdene M.; Xu G.-R.; Batmunkh M.; Bati A.-S.-R.; White J.-J.; Nine M.-J.; Losic D.; Chen Y.; Wang Y.; Ma T.-Y.; Shapter J.-G. Surface Oxidized Two-Dimensional Antimonene Nanosheets for Electrochemical Ammonia Synthesis under Ambient Conditions. *J. Mater. Chem. A* **2020**, *8*, 4735–4739.

(12) Davy H. The Bakerian lecture: On some Chemical Agencies of Electricity. *Philos. Trans. R. Soc. Lond.* 1807, *97*, 1–56.

(13) Sheng W.; Zhuang Z.; Gao M.; Zheng J.; Chen J.G.; Yan Y. Correlating Hydrogen Oxidation and Evolution Activity on Platinum at Different pH with Measured Hydrogen Binding Energy. *Nat. Commun.* **2015**, *6*, 5848.

(14) Back S.; Jung Y. On the Mechanism of Electrochemical Ammonia Synthesis on the Ru Catalyst. *Phys. Chem. Chem. Phys.* **2016**, *18*, 9161–9166.

(15) Bao D.; Zhang Q.; Meng F.-L.; Zhong H.-X.; Shi M.-M.; Zhang Y.; Yan J.-M.; Jiang Q.; Zhang X.-B. Electrochemical Reduction of N_2 under Ambient Conditions for Artificial N_2 Fixation and Renewable Energy Storage Using N_2/NH_3 Cycle. *Adv. Mater.* **2017**, *29*, 1604799.

(16) Lindley B.-M.; Bruch Q.-J.; White P.-S.; Hasanayn F.; Miller A.-J. Ammonia Synthesis from a Pincer Ruthenium Nitride via Metal–Ligand Cooperative Proton-Coupled Electron Transfer. *J. Am. Chem. Soc.* **2017**, *139*, 5305–5308.

(17) Pickett C.-J.; Talarmin J. Electrosynthesis of Ammonia. *Nature* **1985**, *317*, 652–653.

(18) Shi M.-M.; Bao D.; Wulan B.-R.; Li Y.-H.; Zhang Y.-F.; Yan J.-M.; Jiang Q. Au Sub-Nanoclusters on TiO₂ toward Highly Efficient and Selective Electrocatalyst for N₂ Conversion to NH₃ at Ambient Conditions. *Adv. Mater.* **2017**, *29*, 1606550.

(19) Hao Y.-C.; Guo Y.; Chen L.-W.; Shu M.; Wang X.-Y.; Bu T.-A.; Gao W.-Y.; Zhang N.; Su X.; Feng X.; Zhou J.-W.; Wang B.; Hu C.-W.; Yin A.-X.; Si R.; Zhang Y.-W.; Yan C.-H. Promoting Nitrogen Electroreduction to Ammonia with Bismuth Nanocrystals and Potassium Cations in Water. *Nat. Catal.* **2019**, *2*, 448–456.

(20) Li L.-Q.; Tang C.; Xia B.-Q.; Jin H.-Y.; Zheng Y.; Qiao S.-Z. Two-Dimensional Mosaic Bismuth Nanosheets for Highly Selective Ambient Electrocatalytic Nitrogen Reduction. *ACS Catal.* **2019**, *9*, 2902–2908.

(21) Fu Y.; Richardson P.; Li K.-K.; Yu H.; Yu B.; Donne S.; Kisi E.; Ma T.-Y. Transition Metal Aluminum Boride as a New Candidate for Ambient-Condition Electrochemical Ammonia Synthesis. *Nano-Micro Lett.* **2020**, *12*, 65.

(22) Cui Q.-Y.; Qin G.-Q.; Wang W.-H.; Geethalakshmi K.-R.; Du A.-J.; Sun Q. Mo-based 2D MOF as a Highly Efficient Electrocatalyst for Reduction of N₂ to NH₃: a Density Functional Theory Study. *J. Mater. Chem. A* **2019**, *7*, 14510–14518.

(23) Fukushima T.; Drisdell W.; Yano J.; Surendranath Y. Graphite-Conjugated Pyrazines as Molecularly Tunable Heterogeneous Electrocatalysts. *J. Am. Chem. Soc.* **2015**, *137*, 10926–10929.

- (24) Oh S.; Gallagher J.-R.; Miller J.-T.; Surendranath Y. Graphite-Conjugated Rhenium Catalysts for Carbon Dioxide Reduction. *J. Am. Chem. Soc.* **2016**, *138*, 1820–1823.
- (25) Wu H.-H.; Gong Q.-H.; Olson D.-H.; Li J. Commensurate Adsorption of Hydrocarbons and Alcohols in Microporous Metal Organic Frameworks. *Chem. Rev.* **2012**, *112*, 836–868.
- (26) He Y.; Zhou W.; Qian G.; Chen B. Methane storage in metal–organic frameworks. *Chem. Soc. Rev.* **2014**, *43*, 5657–5678.
- (27) Lee J.; Farha O.-K.; Roberts J.; Scheidt K.-A.; Nguyen S.-T.; Hupp J.-T. Metal–Organic Framework Materials as Catalysts. *Chem. Soc. Rev.* **2009**, *38*, 1450–1459.
- (28) Li J. R.; Kuppler R. J.; Zhou H. C. Selective Gas Adsorption and Separation in Metal–Organic Frameworks. *Chem. Soc. Rev.* **2009**, *38*, 1477–1504.
- (29) Gao G.; Zheng F.; Pan F.; Wang L.-W. Theoretical Investigation of 2D Conductive Microporous Coordination Polymers as Li–S Battery Cathode with Ultrahigh Energy Density. *Adv. Energy Mater.* **2018**, *8*, 1801823.
- (30) Fujita M.; Kwon Y.-J.; Washizu S.; Ogura K. Preparation, Clathration Ability, and Catalysis of a Two-Dimensional Square Network Material Composed of Cadmium(II) and 4,4'-Bipyridine. *J. Am. Chem. Soc.* **1994**, *116*, 1151–1152.
- (31) Chughtai A.-H.; Ahmad N.; Younus H. A.; Laypkov A.; Verpoort F. Metal–Organic Frameworks: Versatile Heterogeneous Catalysts for Efficient Catalytic Organic Transformations. *Chem. Soc. Rev.* **2015**, *44*, 6804–6849.
- (32) Dhakshinamoorthy A.; Asiri A.-M.; Garcia H. Metal-Organic Framework (MOF) Compounds: Photocatalysts for Redox Reactions and Solar Fuel Production. *Angew. Chem. Int. Ed.* **2016**, *55*, 5414–5445.

(33) Tian Y.; Wang Y.; Yan L.; Zhao J.; Su Z. Electrochemical reduction of carbon dioxide on the two-dimensional $M_3(\text{Hexaiminotriphenylene})_2$ sheet: A computational study. *Appl. Surf. Sci.* **2019**, *467*, 98–103.

(34) Miner E. M.; Gul S.; Ricke N. D.; Pastor E.; Yano J.; Yachandra V. K.; Van Voorhis T.; Dinca M. Mechanistic Evidence for Ligand-Centered Electrocatalytic Oxygen Reduction with the Conductive MOF $Ni_3(\text{hexaiminotriphenylene})_2$. *ACS Catal.* **2017**, *7*, 7726–7731.

(35) Luo S.-J.; Li X.-M.; Zhang B.-H.; Luo Z.-L.; Luo M. MOF-Derived $Co_3O_4@NC$ with Core-Shell Structures for N_2 Electrochemical Reduction under Ambient Conditions. *ACS Appl. Mater. Interfaces* **2019**, *11*, 26891–26897.

(36) Yoon J.-W.; Seo Y.-K.; Hwang Y.-K.; Chang J.-S.; Leclerc H.; Wuttke S.; Bazin P.; Vimont A.; Daturi M.; Bloch E.; Llewellyn P.-L.; Serre C.; Horcajada P.; Grenèche J.-M.; Rodrigues A.-E.; Férey G. Controlled Reducibility of a Metal–Organic Framework with Coordinatively Unsaturated Sites for Preferential Gas Sorption. *Angew. Chem. Int. Ed.* **2010**, *49*, 4959–4962.

(37) Volkringer C.; Leclerc H.; Lavalley J.-C.; Loiseau T.; Férey G.; Daturi M.; Vimont A. Infrared Spectroscopy Investigation of the Acid Sites in the Metal–Organic Framework Aluminum Trimesate MIL-100(Al). *J. Phys. Chem. C* **2012**, *116*, 5710–5719.

(38) Férey G.; Mellot-Draznieks C.; Serre C.; Millange F.; Dutour J.; Surblé S.; Margiolaki I. A Chromium Terephthalate-Based Solid with Unusually Large Pore Volumes and Surface Area. *Science* **2005**, *309*, 2040–2042.

(39) Yoon J.-W.; Chang H.; Lee S.-J.; Hwang Y.-K.; Hong D.-Y.; Lee S.-K.; Lee J.-S.; Jang S.; Yoon T.-U.; Kwac K.; Jung Y.; Pillai R.-S.; Faucher F.; Vimont A.; Daturi M.; Férey G.; Serre C.; Maurin G.; Bae Y.-S.; Chang J.-S. Selective Nitrogen Capture by Porous Hybrid Materials Containing Accessible Transition Metal Ion Sites. *Nat. Mater.* **2017**, *16*, 526–531.

(40) Volkringer C.; Popov D.; Loiseau T.; Férey G.; Burghammer M.; Riekel C.; Haouas M.; Taulelle F. Synthesis, Single-Crystal X-ray Microdiffraction, and NMR Characterizations of the Giant Pore Metal-Organic Framework Aluminum Trimesate MIL-100. *Chem. Mater.* **2009**, *21*, 5695–5697.

(41) Horcajada P.; Surblé S.; Serre C.; Hong D.-Y.; Seo Y.-K.; Chang J.-S.; Grenèche J.-M.; Margiolaki I.; Férey G. Synthesis and Catalytic Properties of MIL-100(Fe), an Iron(III) Carboxylate with Large Pores. *Chem. Commun.* **2007**, 2820–2822.

(42) Cai J.-H.; Mao X.-H.; Song W.-G. Adsorption Behavior and Structure Transformation of Mesoporous Metal–Organic Frameworks towards Arsenates and Organic Pollutants in Aqueous Solution. *Mater. Chem. Front.* **2018**, *2*, 1389.

(43) Zhang F.-M.; Shi J.; Jin Y.; Fu Y.-H.; Zhong Y.-J.; Zhu W.-D. Facile Synthesis of MIL-100(Fe) under HF-Free Conditions and its Application in the Acetalization of Aldehydes with Diol. *Chem. Eng. J.* **2015**, *259*, 183–190.

(44) Zou Y.; Yan F.-Y.; Dai L.-F.; Luo Y.-M.; Fu Y.; Yang N.; Wun J.-Y.; Chen L. High Photoluminescent Carbon Nanodots and Quercetin- Al^{3+} Construct a Ratiometric Fluorescent Sensing System. *Carbon* **2014**, *77*, 1148–1156.

(45) Kumar N.; Biswas K. Cryomilling: An Environment Friendly Approach of Preparation Large Quantity Ultra Refined Pure Aluminium Nanoparticles. *J. Mater. Res. Technol.* **2019**, *8*, 63–74.

(46) Matanovic I.; Garzon H.-F. Nitrogen Electroreduction and Hydrogen Evolution on Cubic Molybdenum Carbide: A Density Functional Study. *Phys. Chem. Chem. Phys.* **2018**, *20*, 14679–14687.

(47) Choi C.; Back S.; Kim N.-Y.; Lim J.; Kim Y.-H.; Jung Y. Suppression of Hydrogen Evolution Reaction in Electrochemical N₂ Reduction Using Single-Atom Catalysts: A Computational Guideline. *ACS Catal.* **2018**, *8*, 7517–7525.

(48) Han L.-L.; Liu X.-J.; Chen J.-P.; Lin R.-Q.; Liu H.-X.; Lu F.; Bak S.; Liang Z.-X.; Zhao S.-Z.; Stavitski E.; Luo J.; Adzic R.-R.; Xin H.-L. Atomically Dispersed Molybdenum Catalysts for Efficient Ambient Nitrogen Fixation. *Angew. Chem. Int. Ed.* **2019**, *58*, 2321–2325.

(49) Luo S.-J.; Li X.-M.; Gao W.-G.; Zhang H.-Q.; Luo M. An MOF-Derived C@NiO@Ni Electrocatalyst for N₂ Conversion to NH₃ in Alkaline Electrolytes. *Sustain. Energy Fuels* **2020**, *4*, 164.

(50) Andersen S.-Z.; Čolić V.; Yang S.; Schwalbe J.-A.; Nielander A.-C. Mc; McEnaney J.-M.; Enemark-Rasmusse K.; Baker J.-G.; Singh A.-R.; Rohr B.-A.; Statt M.-J.; Blair S.-J.; Mezzavilla S.; Kibsgaard J.; Vesborg P.-C.-K.; Cargnello M.; Bent S.-F.; Jaramillo T.-F.; Stephens I.-E.L.; Nørskov J.-K.; Chorkendorff I. A Rigorous Electrochemical Ammonia Synthesis Protocol with Quantitative Isotope Measurements. *Nature* **2019**, *570*, 504–508.

(51) Zhao Y.-X.; Shi R.; Bian X.A.; Zhou C.; Zhao Y.-F.; Zhang S.; Wu F.; Waterhouse G.-I.-N.; Wu L.-Z.; Tung C.-H.; Zhang T.-R. Ammonia Detection Methods in Photocatalytic and Electrocatalytic Experiments: How to Improve the Reliability of NH₃ Production Rates? *Adv. Sci.* **2019**, *6*, 1802109.

(52) Yang C.-X.; Ren H.-B.; Yan X.-P. Fluorescent Metal-Organic Framework MIL-53(Al) for Highly Selective and Sensitive Detection of Fe³⁺ in Aqueous Solution. *Anal. Chem.* **2013**, *85*, 7441-7446.

(53) Shearer C.-G.; Chavan S.; Bordiga S.; Svelle S.; Olsbye U.; Lillerud P.-K. Defect Engineering: Tuning the Porosity and Composition of the Metal–Organic Framework UiO-66 via Modulated Synthesis. *Chem. Mater.* **2016**, *28*, 3749–3761.

(54) Shearer G.-C.; Chavan S.; Ethiraj J.; Vitillo J.-G.; Svelle S.; Olsbye U.; Lamberti C.; Bordiga S.; Lillerud K.-P. Tuned to Perfection: Ironing Out the Defects in Metal–Organic Framework UiO-66. *Chem. Mater.* **2014**, *26*, 4068–4071.

(55) Ishizaki M.; Akiba S.; Ohtani A.; Hoshi Y.; Ono K.; Matsuba M.; Togashi T.; Kananizuka K.; Sakamoto M.; Takahashi A.; Kawamoto T.; Tanaka H.; Watanabe M.; Arisaka M.; Nankawa T.; Kurihara M. Proton-exchange Mechanism of Specific Cs⁺ Adsorption via Lattice Defect Sites of Prussian Blue Filled with Coordination and Crystallization water Molecules. *Dalton Trans.* **2013**, *42*, 16049–16055.

(56) Fang Z.-L.; Bueken B.; De Vos D.-E.; Fischer R.-A. Defect-Engineered Metal–Organic Frameworks. *Angew. Chem. Int. Ed.* **2015**, *54*, 7234–7254.

(57) Ma H.-Q.; Shi Z.-Y.; Li S.; Liu N. Large-Scale Production of Graphitic Carbon Nitride with Outstanding Nitrogen Photofixation Ability via a Convenient Microwave Treatment. *Appl. Surf. Sci.* **2016**, *379*, 309–315.

(58) Xiang Z.-Y.; Li L.-H.; Wang Y.; Song Y.-L. Recent Advances in Noble-Metal-Free Catalysts for Electrocatalytic Synthesis of Ammonia under Ambient Conditions. *Chem. Asian J.* **2020**, *15*, 1791–1807.

Supporting Information

Unsaturated p-Metal Based Metal-Organic Frameworks for Selective Nitrogen Reduction Under Ambient Conditions

1 Experimental

1.1 Material and chemicals

Nitric acid (HNO_3 , Sigma-Aldrich, > 35%), trimethyl-1,3,5-benzenetricarboxylate (Sigma-Aldrich, 98%), aluminum nitrate nonahydrate ($\text{Al}(\text{NO}_3)_3 \cdot 9\text{H}_2\text{O}$, Sigma-Aldrich, > 98%), terephthalic acid (Sigma-Aldrich, 98%), acetic acid (Sigma-Aldrich), N,N-dimethylformamide (DMF, Sigma-Aldrich, 99.8%), Mo powder (Metco), Al powder (Australian Metal Powders Supplies, > 99 %, 45 μm), Nafion® perfluorinated resin solution (Sigma-Aldrich, 5 wt.%), Nafion® 117 membrane, potassium hydroxide (Sigma-Aldrich, 90%), low level ammonia pH adjusting ISA (Thermo SCIENTIFIC), ammonia standard solution (1000 ppm ammonium chloride, Thermo SCIENTIFIC), phenol (BDH Laboratory Supplies), ammonium sulphate (BDH Chemical, Australia Pty. Ltd.), sodium nitroferricyanide (III) dehydrate (Sigma-Aldrich, > 99 %), trisodium citrate dehydrate (Sigma-Aldrich), sodium hydroxide (Sigma-Aldrich), sodium hypochlorite solution (Sigma-Aldrich), and ethanol (Merck KGaA) were used as received without further purification.

1.2 Material characterizations

Scanning electron microscopy (SEM) images were obtained on a Zeiss Sigma VP FESEM instrument operating at 3 kV after gold sputtering. Energy-dispersive X-ray spectroscopy

(EDS) investigations were conducted using a Bruker EDS detector. Transmission electron microscopy (TEM) was conducted on a JEOL JEM-2100 HRTEM instrument operating at 200 kV, equipped with a JEOL JED-2300 EDS detector. The crystallinity and phase purity of the obtained samples were characterized by X-ray diffraction (XRD) technique, recorded on a Panalytical X'PertTM diffractometer using a Cu-K α radiation. X-ray photoelectron spectroscopy (XPS) measurements were performed by using a Thermo SCIENTIFIC K-Alpha+ X-ray photoelectron spectrometer. A temperature programmed desorption (TPD) was conducted on Belcat II fully-automated catalyst analyzer (MicrotracBEL, Japan). Thermogravimetric analysis (TGA) was performed by using STA 2500 Regulus-NETZSCH thermal analyser. All electrochemical measurements were carried out on a CHI760e electrochemical station. Detection of ammonia was recorded using a spectrophotometer (UV-1800, SHIMADZU).

1.3 Synthesis of electrocatalysts

MIL-100 (Al) Synthesis. Aluminum-based MIL-100 was synthesized according to Volkringer et al [1] via a hydrothermal method using a mixture of Al(NO₃)₃·9H₂O, trimethyl-1,3,5-benzenetricarboxylate (noted as btcMe₃), HNO₃ and ultrapure water. In brief, the composition (Al(NO₃)₃·9H₂O: 1.6345 g, 4.27 mmol; btcMe₃: 0.7386 g, 2.87 mmol; HNO₃: 0.3774 g, 5.39 mmol; H₂O: 20 mL) was placed in a 50 mL Teflon cell in an autoclave. The reaction occurred at 210 °C for 3.5 h in an oven. After cooling down, a yellowish product was collected by filtration, followed by washing with ultrapure water and acetone. In order to obtain an empty pore phase, the activation of MIL-100(Al) was performed by a two-step process using a N,N-dimethylformamide (DMF) and hot water to decrease the amount of residual organics and anions [2]. Typically, 1 g of the yellowish powder and 40 mL of DMF were placed in a 50 ml Parr-type Teflon-lined autoclave and heated at 150 °C for 3 h. After filtrating and drying, a white powder product (MIL-100 (Al)) and 40 mL ultrapure water were

placed in a 50 ml Parr-type Teflon-lined autoclave and heated at 80 °C for 10 h. Then, the sample was collected by filtration, followed by drying at room temperature.

Synthesis of defect aluminum-based MIL-100 (defect MIL-100 (Al)). The synthesis of defect aluminum-based MIL-100 was carried out according to Lillerud et al [3] using a hydrothermal method. Briefly, the mixture ($\text{Al}(\text{NO}_3)_3 \cdot 9\text{H}_2\text{O}$: 1.6345 g, 4.27 mmol; btcMe_3 : 0.7386 g, 2.87 mmol; HNO_3 : 0.3774 g, 5.39 mmol; acetic acid: 1.5385 g, 25.62 mmol; H_2O : 20 mL) was placed in a 50 mL Teflon cell and reacted at 210 °C for 3.5 h in an oven. After cooling down, yellowish product was collected by filtration, and then washed with ultrapure water and acetone, followed by drying at room temperature. Then, the activation of defect MIL-100(Al) was also performed using the same method described above.

MIL-53 (Al) Synthesis. Aluminum-based MIL-53 was synthesized based on previous literatures [4, 5]. The sample was hydrothermally synthesized under autogenous pressure using a mixture of $\text{Al}(\text{NO}_3)_3 \cdot 9\text{H}_2\text{O}$, terephthalic acid (noted H_2BDC), and ultrapure water. The mixture ($\text{Al}(\text{NO}_3)_3 \cdot 9\text{H}_2\text{O}$: 1.6345 g, 4.27 mmol; H_2BDC : 0.4768 g, 2.87 mmol; H_2O : 30 mL) was placed in a 50 mL Teflon cell in an autoclave and reacted at 210 °C for 24 h in an oven. After cooling down, a white product was collected by filtration, and washed with ultrapure water and acetone, followed by drying at room temperature.

1. 4 Preparation of the electrode

0.25 g of the catalyst material was suspended in 9 mL ethanol and 1 mL Nafion® based aqueous solution (5 wt%). The solution was then ultrasonicated for 1 h to obtain a uniform solution.

Copper foam electrodes (1 cm^2) were cleaned with 0.1 M HCl, ultrapure water, and acetone using ultrasonication, before being used. After drying, the pre-cleaned electrodes were dipped in the above catalyst ink 3 times. During each dipping steps, the copper foam electrodes were completely covered with the ink. The coated electrode was then placed in an oven at 100 °C

for 5 min. A Nafion® 117 membrane was cut into small pieces and then treated with 3 wt% H₂O₂ solution, ultrapure water, 1 mol/L H₂SO₄, and deionized water for 1 h at 80 °C. The obtained membranes were repeatedly rinsed with water until neutral pH was obtained.

1.5 Electrochemical measurements

All electrochemical measurements were carried out in a three electrode system with Pt wire as the counter electrode, Ag/AgCl (3.5 M KCl) as the reference electrode, and catalyst coated copper foam as the working electrode. The gas-tight two-compartment electrochemical cell was separated by a piece of Nafion® 117 membrane. 250 mL/min of N₂ (99.99%) was introduced to the cathodic side of the system 30 min prior to starting the catalytic reaction and also during the reaction. The reaction was carried out in room temperature under ambient conditions. All of the potentials in this work were calculated to a reversible hydrogen electrode (RHE) scale based on the Nernst equation ($E_{RHE} = E_{Ag/AgCl} + 0.059 \times \text{pH} + 0.2046$). The value of 0.2046 depended on the KCl concentration in the reference electrode.

2 Calculations

1). Ammonia yields were calculated using the following equation:

$$R_{NH_3} (\mu g h^{-1} cm^{-2} mg_{cat}^{-1}) = \frac{c (ppb) \times V(L)}{t(h) \times S(cm^2) \times m(mg)}$$

where:

$R_{NH_3} (\mu g h^{-1} cm^{-2} mg_{cat}^{-1})$: Ammonia formation yield

c (ppb): Ammonia concentration in the detection solution in ppb ($\mu g/L$)

V (L): Volume of solution in liters

t (h): Reaction time in hours

S (cm²): Active area of the membrane electrode in cm²

m (mg): Mass of catalysts in milligram

2) Faraday efficiency of ammonia was determined using the following equation:

$$FE(\%) = \frac{3 \times c \text{ (ppb)} \times 10^{-6} \times V \text{ (L)} \times F}{17 \times Q \text{ (C)}} \times 100 \%$$

Where:

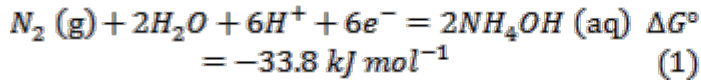
F: Faraday constant in C/mol;

Q: Total quantity of electric charge in C.

3) Calculation of the equilibrium potential [6]:

The standard potential for the half reaction of N₂ reduction to NH₄OH was calculated according to the standard molar Gibbs energy of formation at 298.15 K [7].

The equilibrium potential under our experimental conditions is calculated using the Nernst equation, assuming 1 atm of N₂ and a NH₄OH concentration of 0.0078 mM/L (measured at the optimal applied potential of 0.00 V vs. RHE) in the solution.



$$E^\circ = -\frac{\Delta G^\circ}{nF} = 0.058 \text{ V}, \text{ where } n = 6 \text{ is the number of electrons transferred in the reaction and}$$

F is the Faraday constant.

The equilibrium potential under our experimental conditions is calculated using the Nernst equation, assuming 1 atm of N₂ and a 0.0078 mM/L concentration of NH₄OH in the solution.

$$\begin{aligned} E_{\text{equilibrium}} \text{ (vs. RHE)} &= E^\circ - \frac{RT}{6F} \ln \left(\frac{[NH_4OH]^2}{[H^+]^6} \right) + 0.059 \times pH \\ &= 0.177 \text{ V vs. RHE} \end{aligned} \quad (2)$$

4) Calculation of the overpotential [8]:

$$\begin{aligned} \Delta E &= E_{\text{equilibrium}} \text{ (vs. RHE)} - E_{\text{limiting}} \text{ (vs. RHE)} = 0.177 \text{ V} - 0 \text{ V} = 0.177 \text{ V} \\ &= 177 \text{ mV} \end{aligned} \quad (3)$$

The value of E_{limiting} is equal to the applied potential required to eliminate the energy barrier of the rate-limiting step.

3 Detection of ammonia

Low ammonia concentration detection was carried out by spectrophotometry (indophenol blue method) and/or ion selective electrode analysis (Orion™ High-Performance Ammonia Electrode 9512HPBNWP) methods. In addition, only a single absorber was used in the experiments.

a. Ammonia-selective electrode method

Apparatus: Ammonia ion selective electrode – Ionic Strength Adjuster (Thermo Scientific Orion high performance ammonia ion selective electrode Cat.No.9512HPBNWP); Electrometer.

Procedures:

- a) Preparation of ammonia standards: A series of standard solutions were prepared with the concentrations of 20, 200, and 2000 ppb (NH_4^+) in 0.1 M KOH (absorber).
- b) Electrometer calibration: the following steps were performed during the electrometer calibration:
 - i. The electrode was soaked in an ammonia electrode storage solution for at least 15 min.
 - ii. The meter measurement mode was operated in mV mode.
 - iii. 100 mL of each standard was measured into separate, clean beakers. 2 mL low level ammonia pH-adjusting ionic strength adjuster was added to each beaker prior to calibration, followed by waiting until the reading was stable for 2 min.
 - iv. The mV and ppb values were used as the Y axis and X axis respectively, to prepare the standard curve.
 - v. The electrode slope was checked for validity (slope should be between 54 and 60 in a temperature range of 20-25 °C).
- c) 50 mL sample was measured and 1 mL Low level ammonia pH-adjusting ionic strength adjuster was added. When getting readings which were stable for at least 2 min, the measurement was recorded.
- d) Calculation

b. Indophenol blue method

In addition, for comparison to the ammonia-selective electrode method, a colorimetric method using indophenol blue for NH_3 detection was also performed to confirm the reliability of the former method.

Apparatus: A spectrophotometer (UV-1800, SHIMADZU) was used at fixed wavelength ($\lambda=660$ nm).

Procedures:

a) Preparation of special reagents:

- i. Phenol-alcohol reagent: Dissolve 10 g phenol in 95% ethyl alcohol to a final volume of 100 ml.
- ii. Sodium nitroprusside (nitroferrocyanide): Dissolve 1 g in DI water to a final volume of 200 ml. Store in dark bottle for no more than 1 month.
- iii. Alkaline complexing reagent: Dissolve 100 g trisodium citrate and 5 g sodium hydroxide in DI water to a final volume of 500 ml.
- iv. Oxidizing solution: Add 100 ml alkaline complexing reagent to 25 ml sodium hypochlorite (as fresh as possible).

b) Measurement:

- i. Preparation of NH_3 standards: A series of NH_3 standard solutions were prepared with the concentrations of 0, 50, 100, 200, 500, 750, and 1000 ppb (NH_4^+) by dissolving in $(\text{NH}_4)_2\text{SO}_4$.
- ii. 10 mL of standard or sample solution was taken. Then 400 μL phenol solution, 400 μL nitroferrocyanide solution and 1 ml oxidizing reagent were added to the standard or sample solution. Absorbance measurements of standards and unknown samples were performed at $\lambda=660$ nm using a spectrophotometer after mixing the solutions well for at least 1 h.
- iii. Absorbance values of standards were used to generate a standard curve. The standard

curve below was used to calculate the ammonia concentration in unknown solutions.

As shown in Figure S15, with gradual increasing of the addition NH_3 concentration, a new absorption band centered at 660 nm appeared with increasing intensity, accompanied by a clear color change from colorless to blue. In addition, an almost perfect linearity was observed between NH_3 concentration and absorbance in Figure S16.

c. Determination of hydrazine hydrate

In addition, due to existing by-products, the yield of hydrazine in the electrolyte was examined by the method of Watt and Chrisp [9]. A color reagent was prepared by a mixture of para-(dimethylamino) benzaldehyde (5.99 g), HCl (concentrated, 30 mL) and ethanol (300 mL). A calibration curve was plotted as follows: First, preparing a series of standard solutions with the concentrations of 0, 50, 100, 200, and 500 ppb by pipetting suitable volumes of the hydrazine hydrate-nitrogen 0.1 M KOH solution. Then, the absorbance of the standard or sample solution was measured at $\lambda=460$ nm after mixing 5 mL of standard or sample solution with 5 mL of color reagent. Finally, the yields of hydrazine in unknown sample solutions were estimated from a standard curve.

Figure S17 shows a new absorption band centered at 460 nm appeared with gradual increasing of the addition N_2H_4 concentration corresponding to increasing intensity. Meanwhile, the color of solution changes from colorless to yellow. It exhibits a good linear relation between N_2H_4 concentration and absorbance in Figure S18.

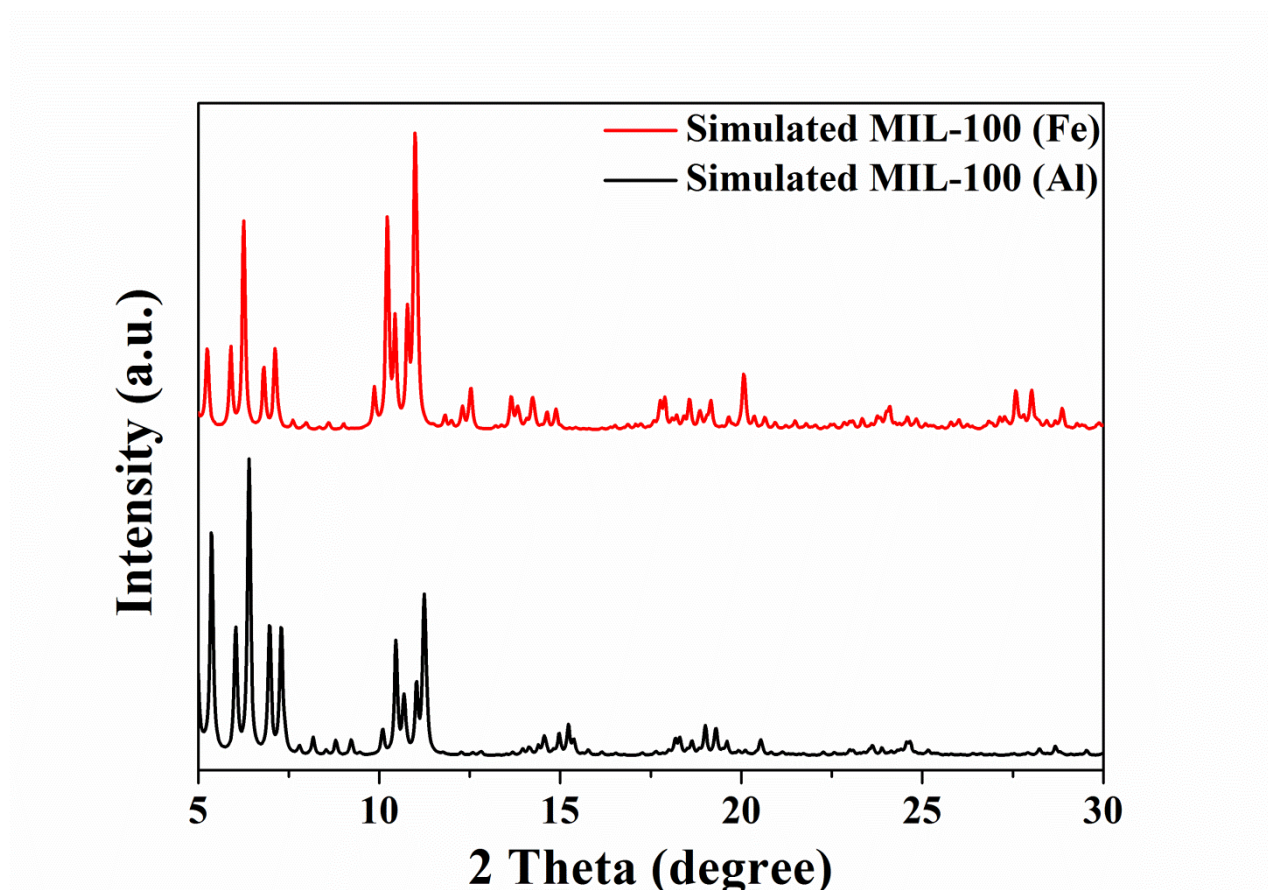


Figure S1 Stand simulated XRD patterns of MIL-100 (Al) and MIL-100 (Fe) derived from Mercury software.

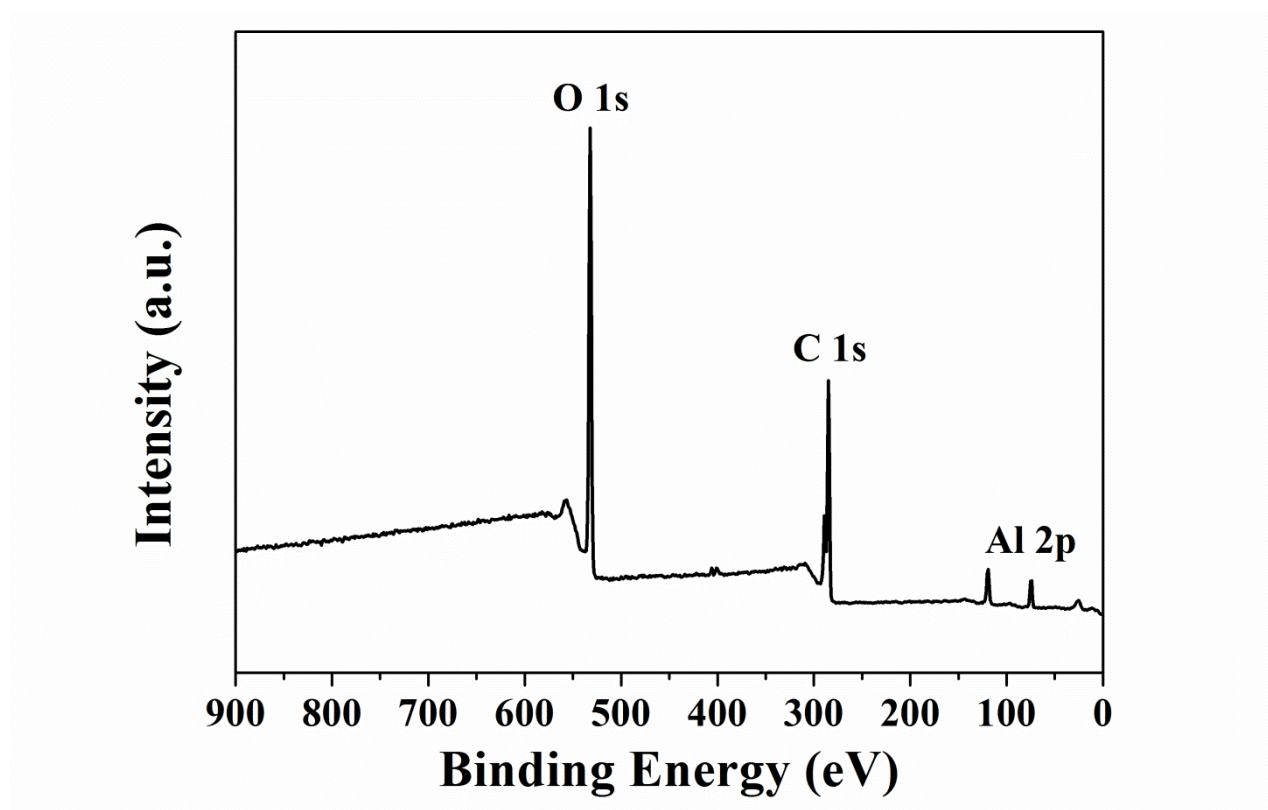


Figure S2 XPS spectrum for MIL-100 (Al).

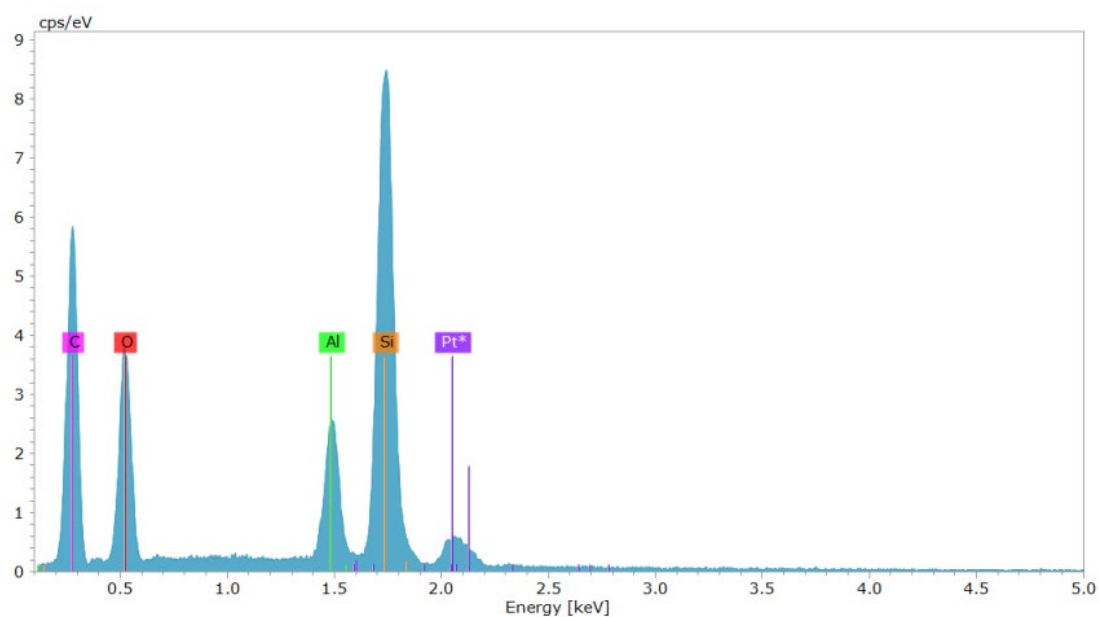


Figure S3 EDS point analysis of the MIL-100 (Al).

Table 1 The amounts of elements atom and weight by EDS.

Element	series	wt. %	at. %
Carbon	K-series	61.58	69.52
Oxygen	K-series	32.41	27.47
Aluminium	K-series	6.01	3.01
	Sum:	100	100

The EDS analysis confirms the presence of C, O and Al (atomic abundance of 69.52%, 27.47% and 3.01%, respectively), which is consistent with of the XPS results. Note: the Pt atom is from the coating and Si is from the substrate.

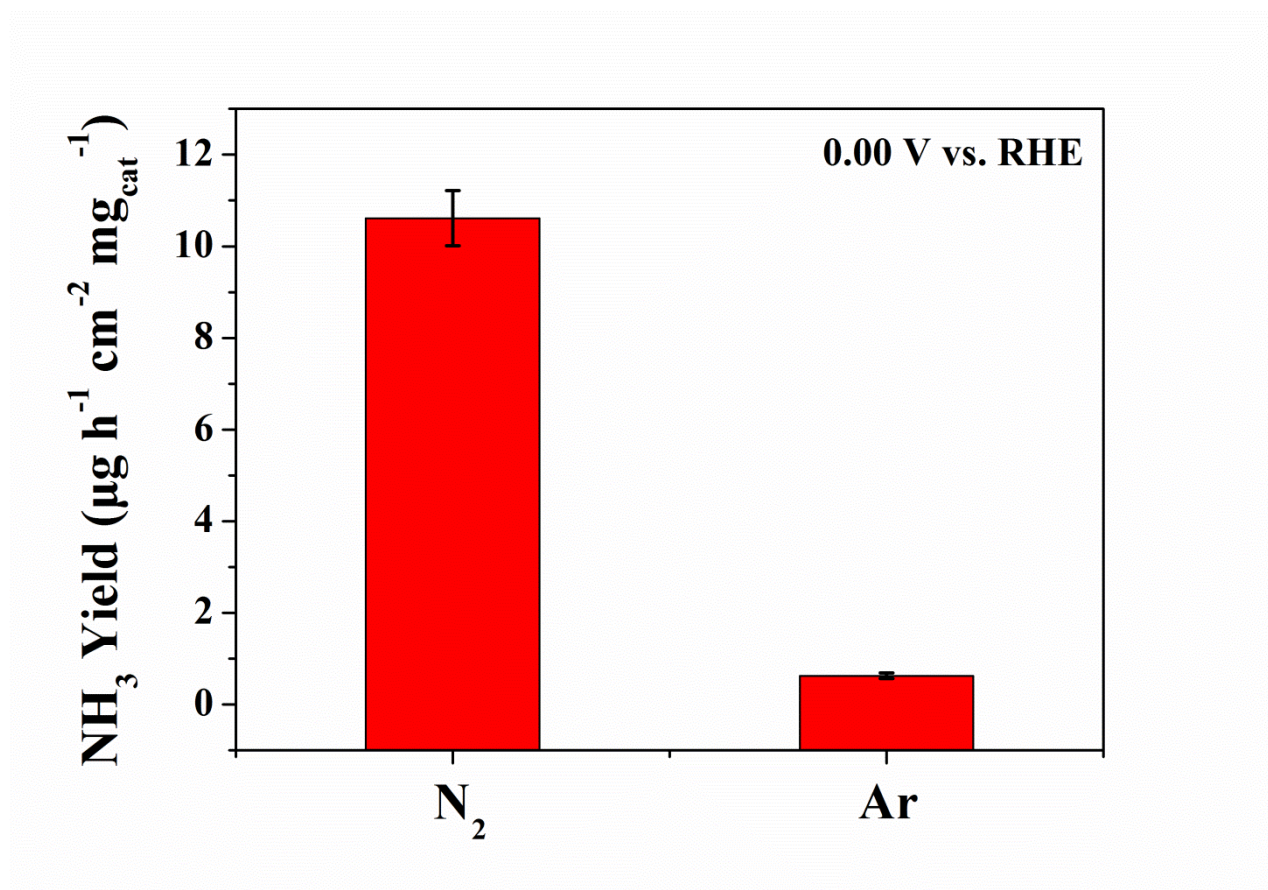


Figure S4 Ammonia yields for the MIL-100 (Al)/Cu foam electrode in an N_2 and Ar-saturated aqueous solution of 0.1 M KOH.

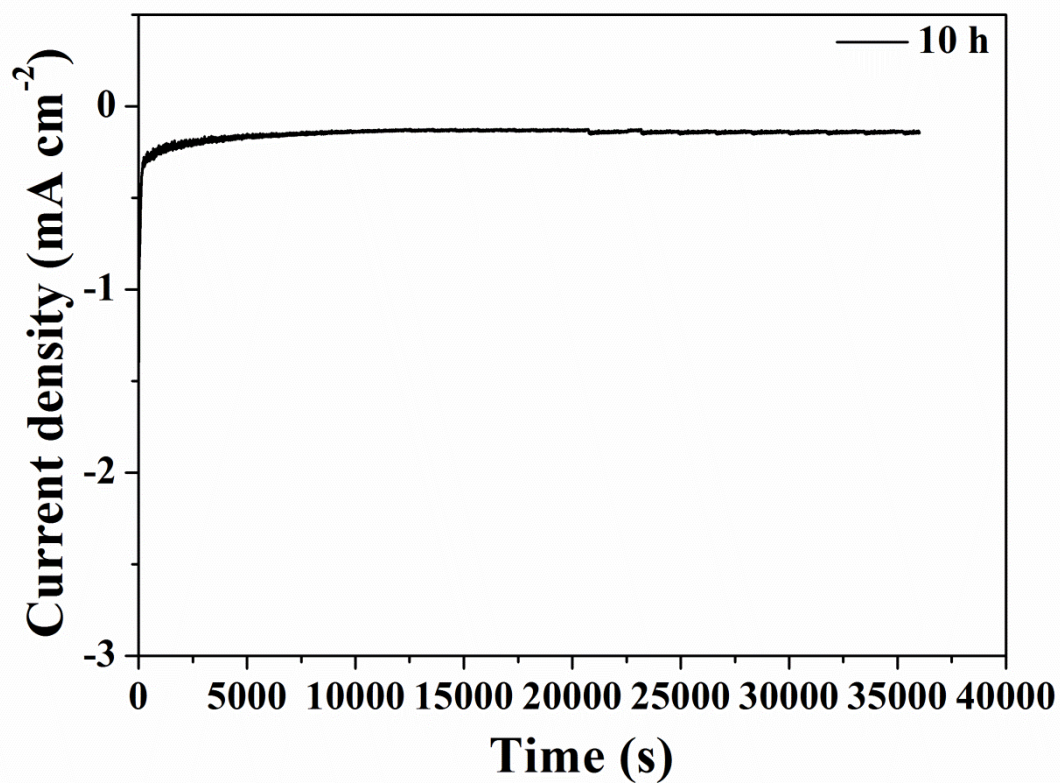


Figure S5 Chronoamperometry results at the 0.00 V vs. RHE over 10 h test.

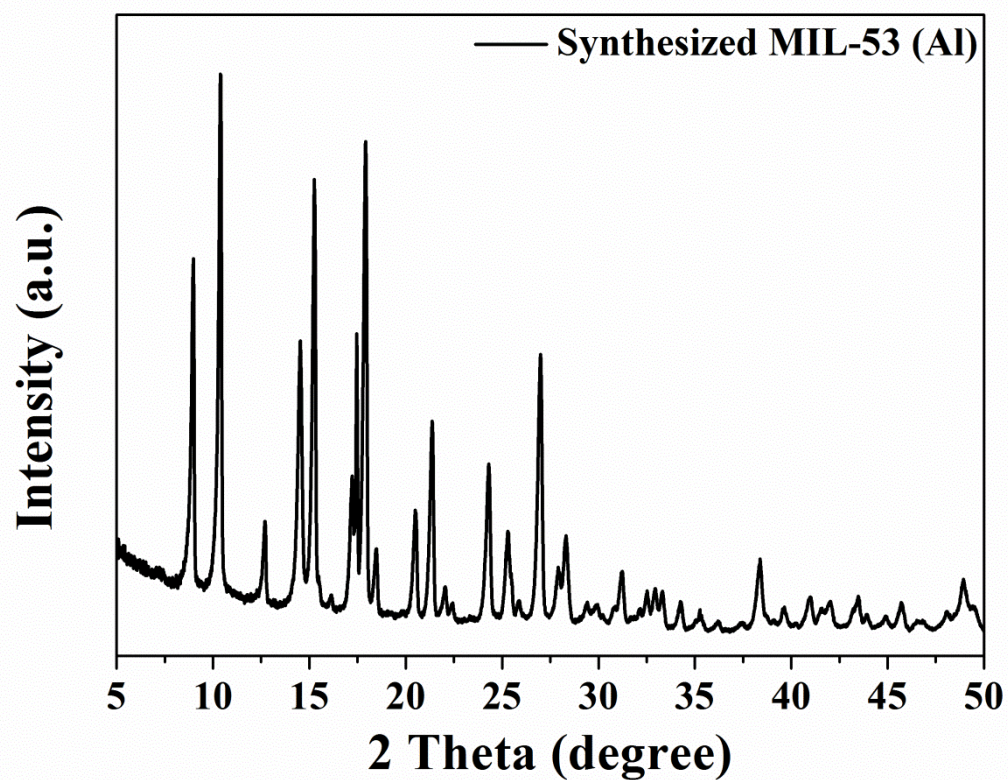


Figure S6 XRD pattern of the MIL-53 (Al).

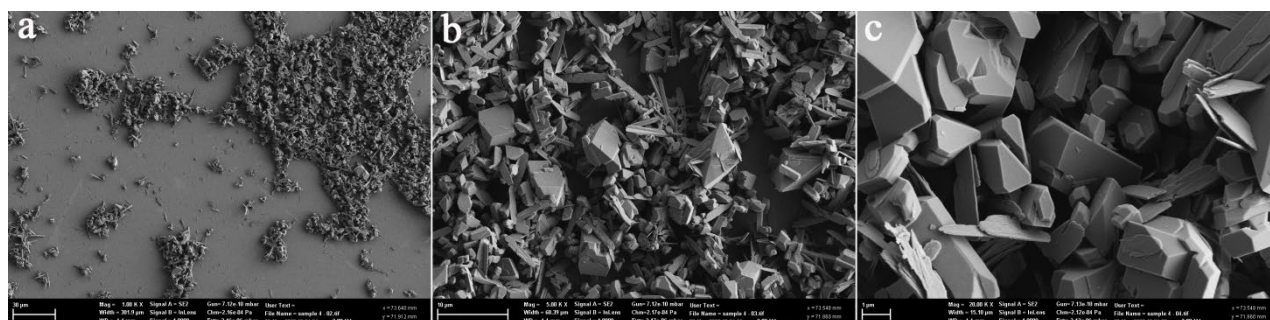


Figure S7 SEM images of the MIL-53 (Al).

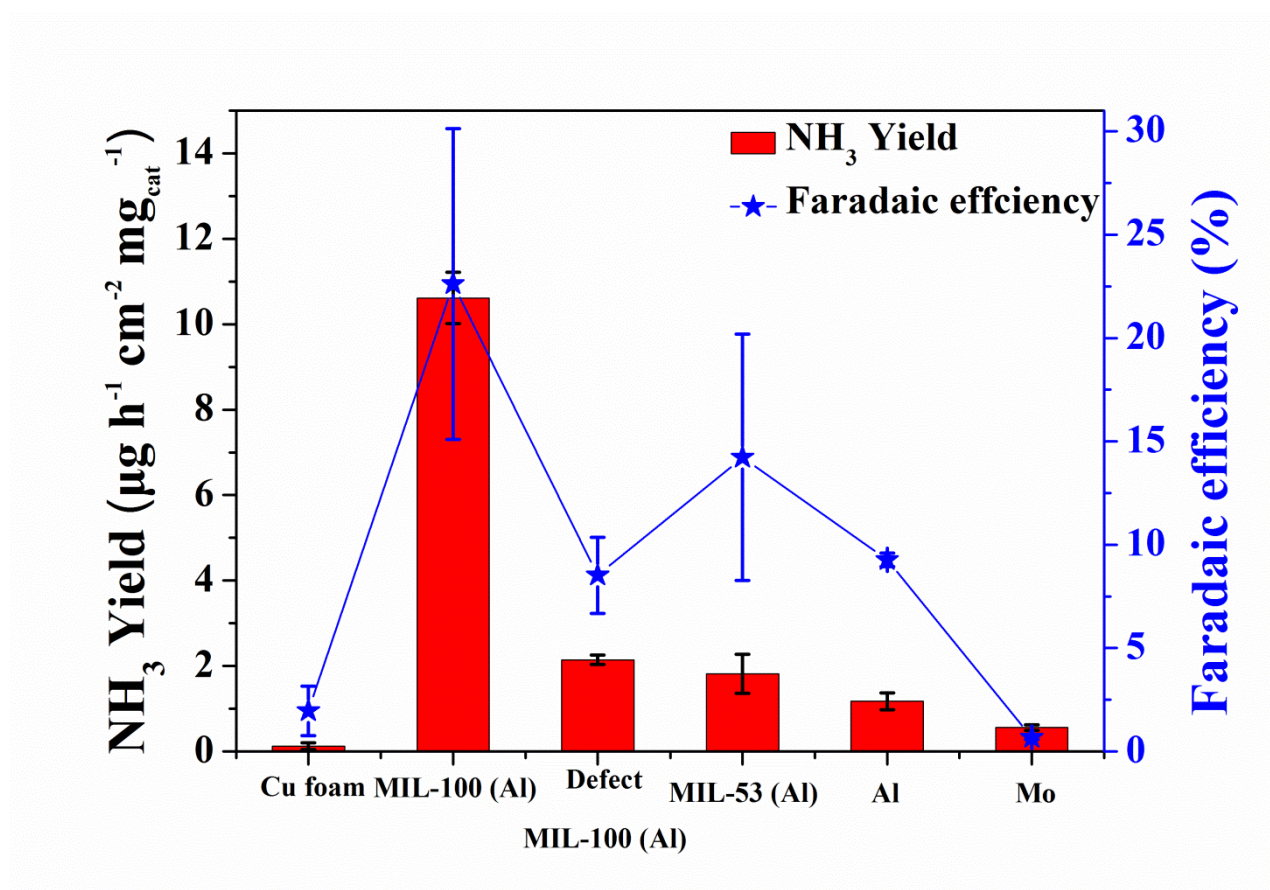


Figure S8 Comparison of ammonia yield and Faradaic efficiencies at 0.00 V vs. RHE for pure Cu foam, MIL-100 (Al), defect MIL-100 (Al), MIL-53 (Al), Al powder, and Mo powder electrodes in an N₂-saturated aqueous solution of 0.1 M KOH.

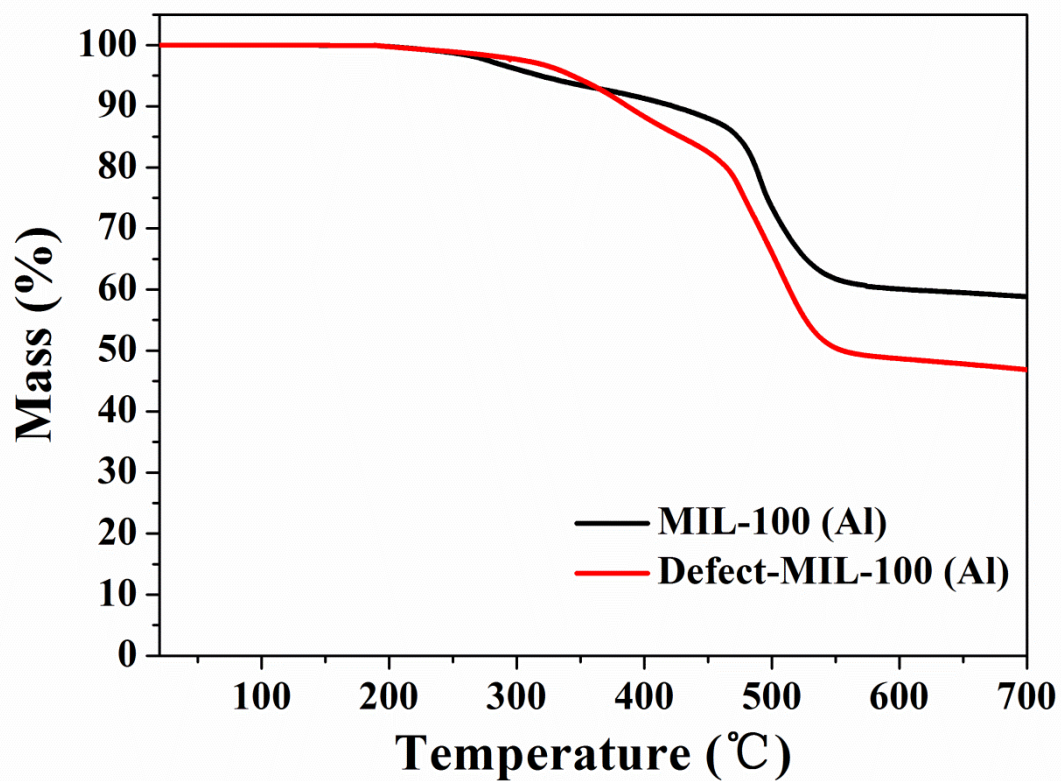


Figure S9 TGA of the MIL-100 (Al) and defect MIL-100 (Al)

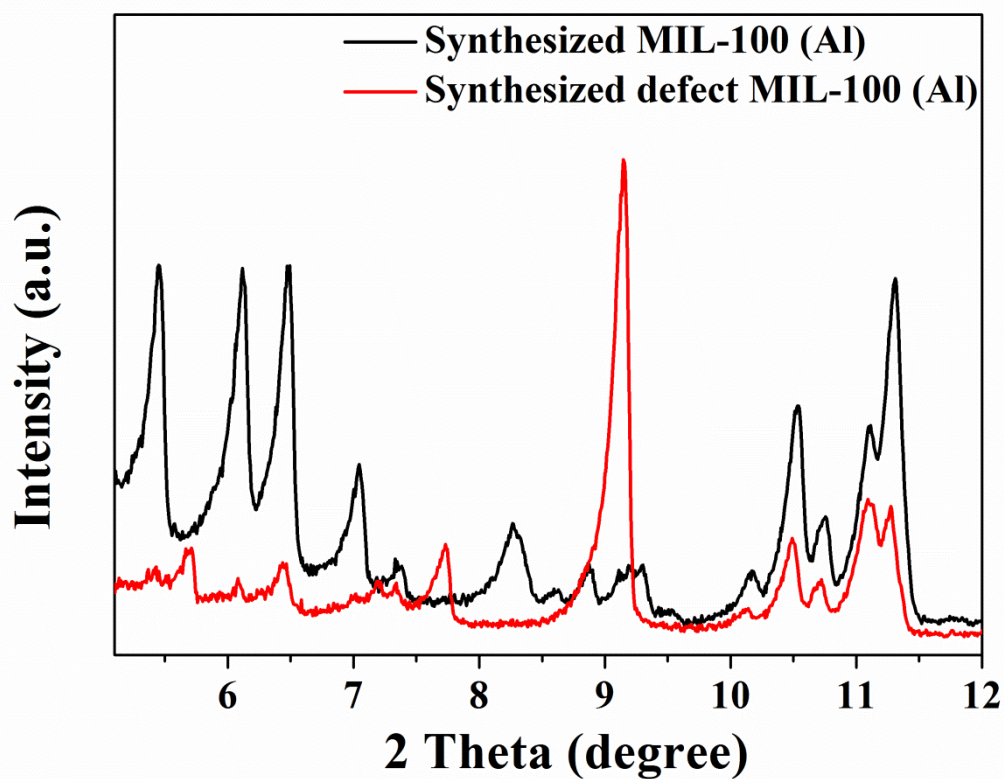


Figure S10 Low-angle ($2\theta=5\text{-}12^\circ$) region of the XRD patterns obtained on the MIL-100 (Al) and defect MIL-100 (Al) samples

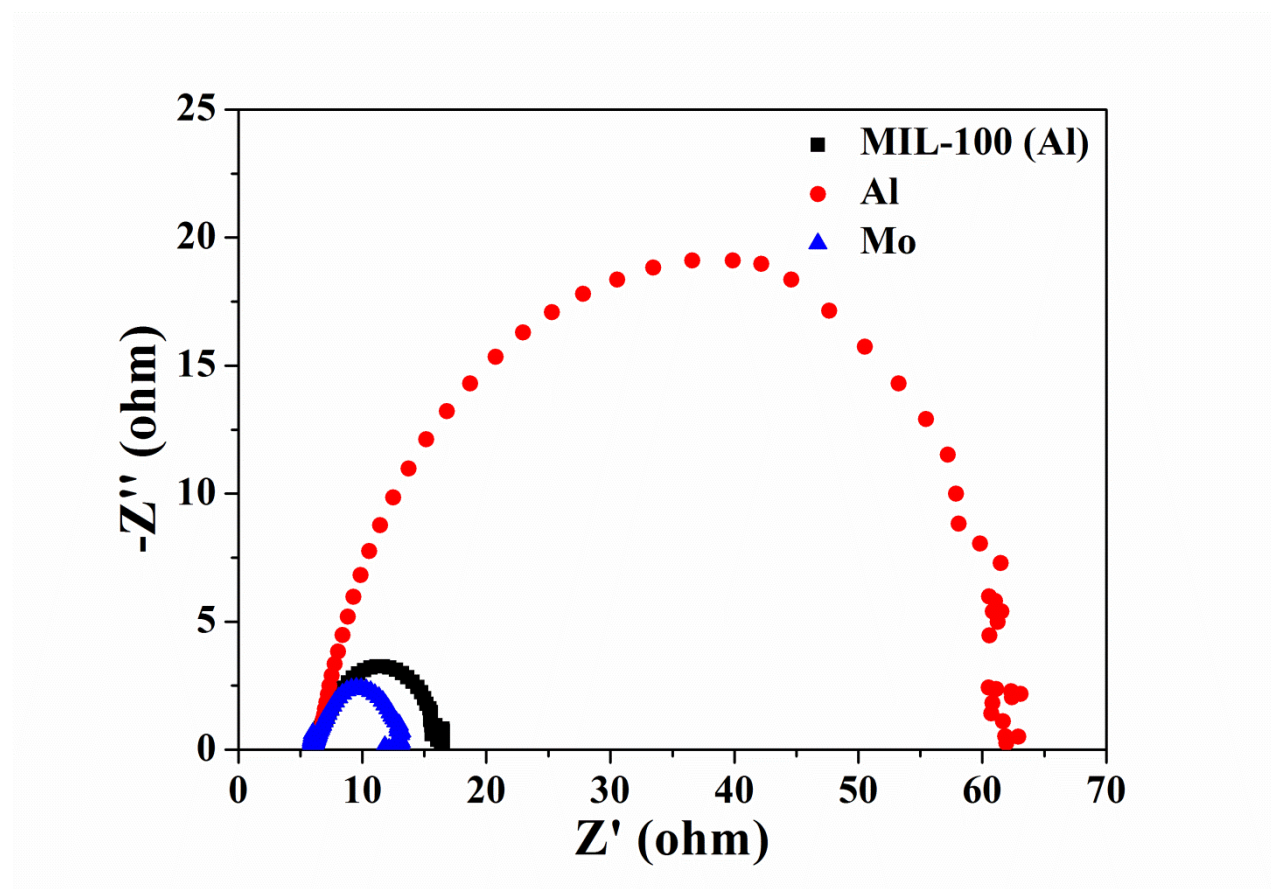


Figure S11 EIS (recorded at -0.3 V vs RHE with inset showing the equivalent circuit diagram) of MIL-100 (Al), Al, and Mo in an N_2 -saturated aqueous solution of 0.1 M KOH.

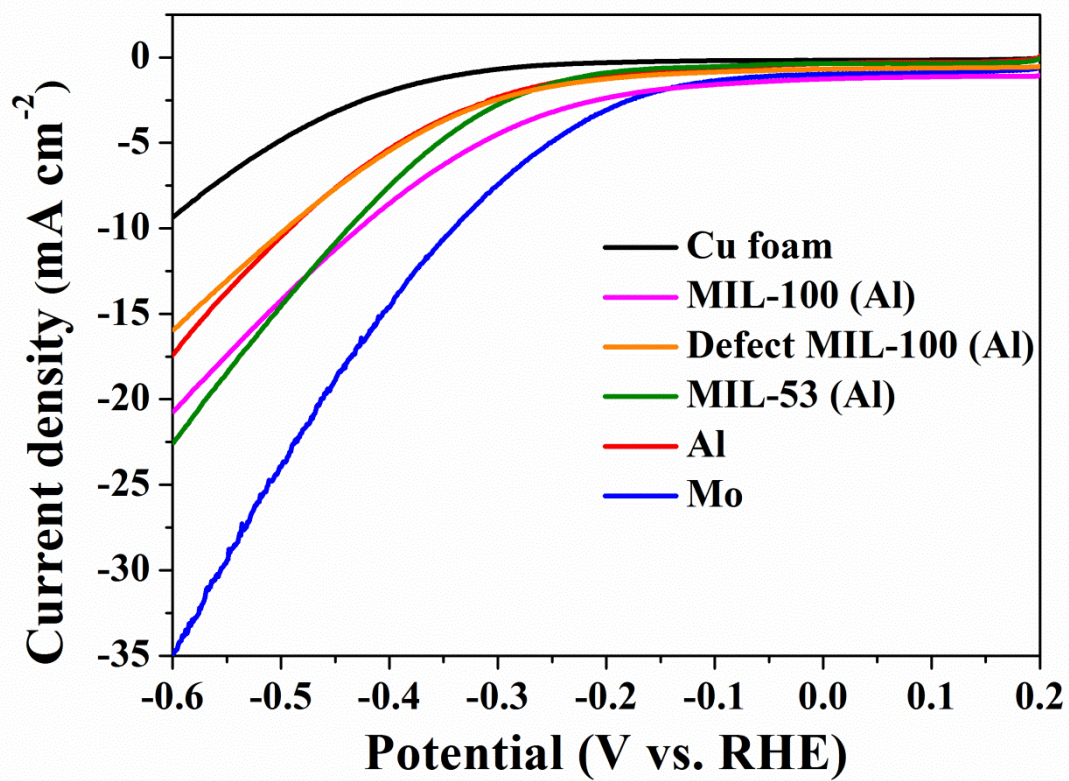


Figure S12 LSV curves of pure Cu foam, MIL-100 (Al), defect MIL-100 (Al), MIL-53 (Al), Al powder, and Mo powder electrode in an N₂-saturated aqueous solution of 0.1 M KOH.

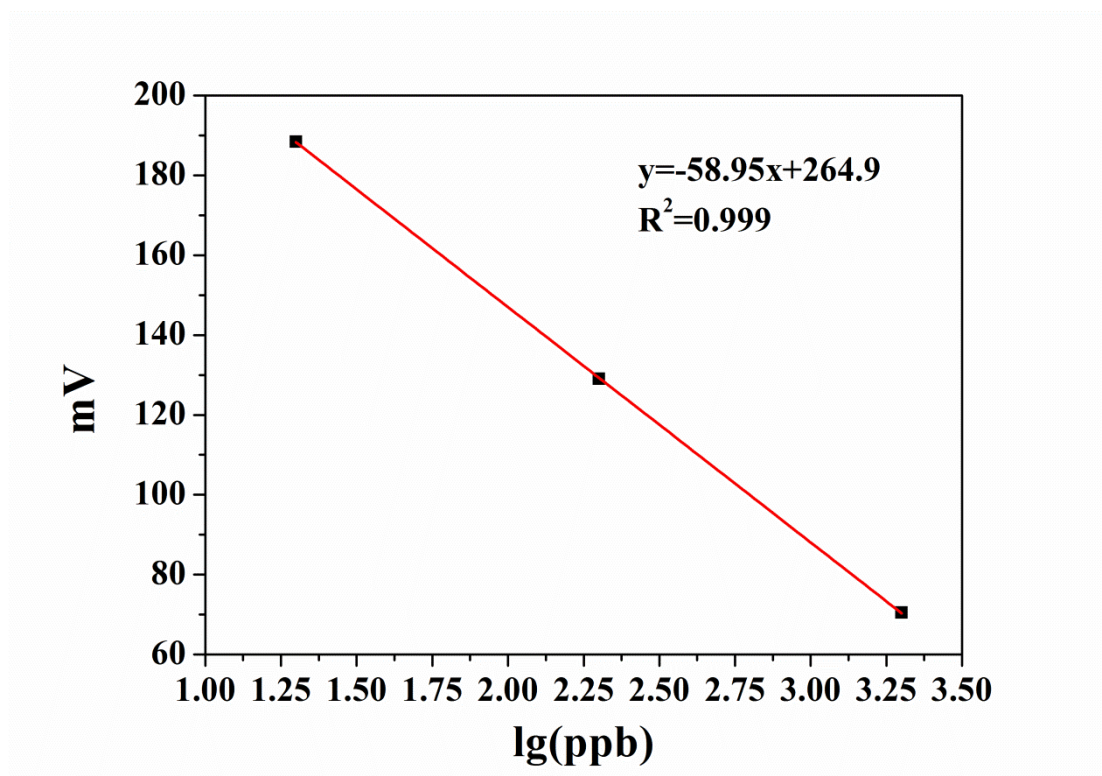


Figure S13 Calibration of NH₃ in 0.1M KOH from 20 ppb to 2000 ppb.



Figure S14 A photograph of ammonia-sensitive testing instrument.

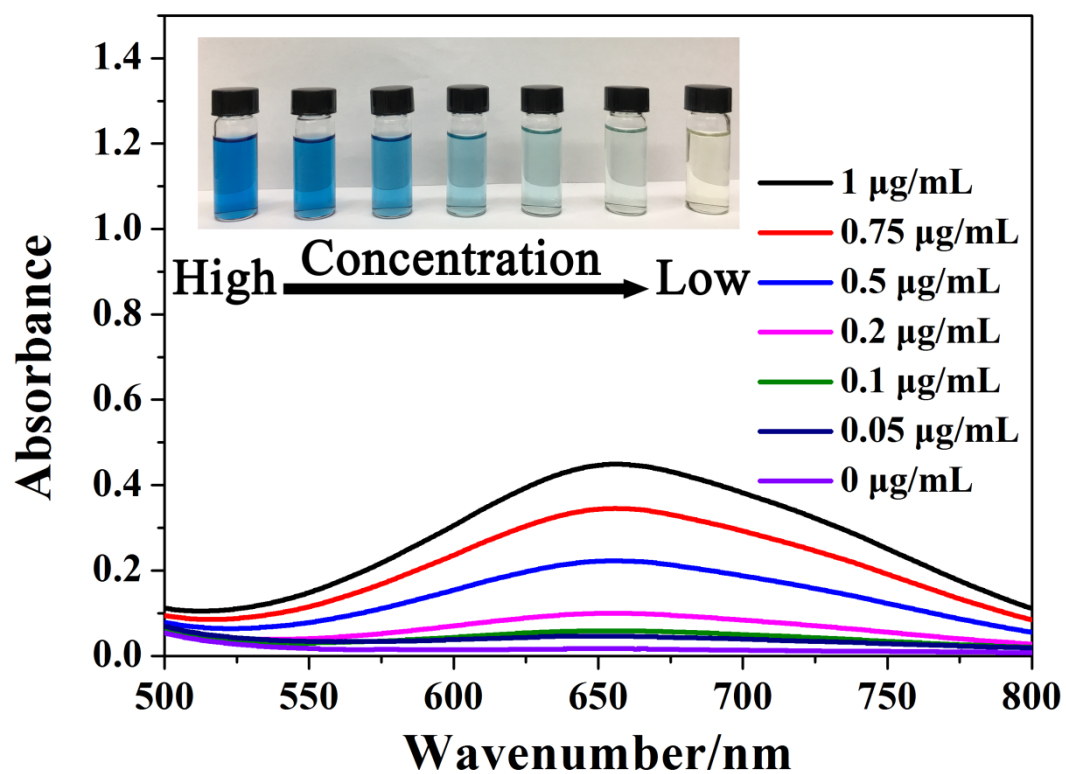


Figure S15 UV-vis curves of various NH_3 concentration based on Indophenol blue method, and the insert shows the chromogenic reaction of Indophenol blue indicator with NH_3 .

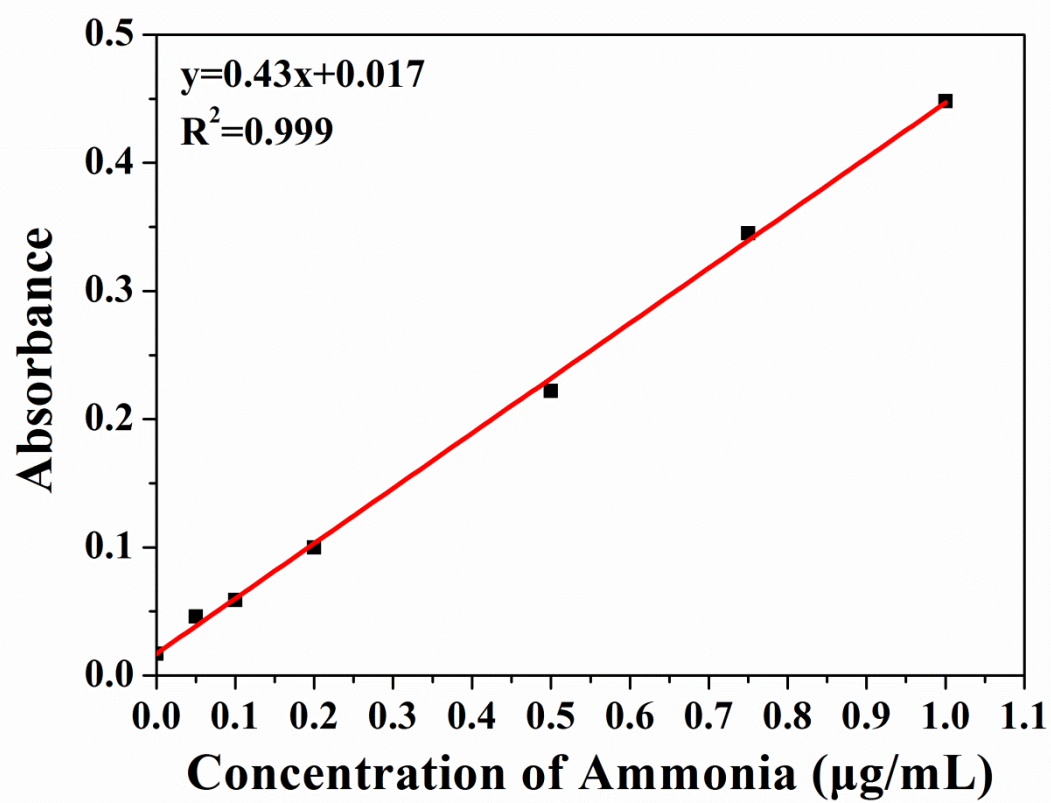


Figure S16 Calibration curve for colorimetric NH_3 assay using the Indophenol blue method.

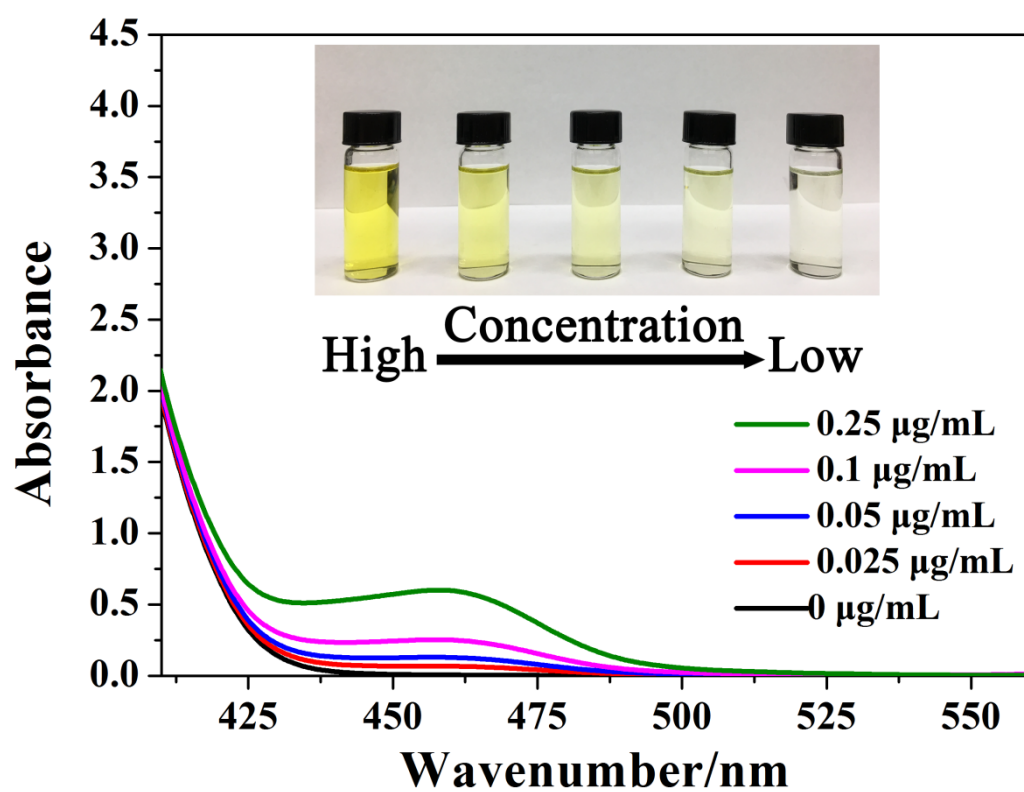


Figure S17 UV-vis curves of various N_2H_4 concentrations, and the insert shows the chromogenic reaction of para-dimethylamino-benzaldehyde indicator with N_2H_4 .

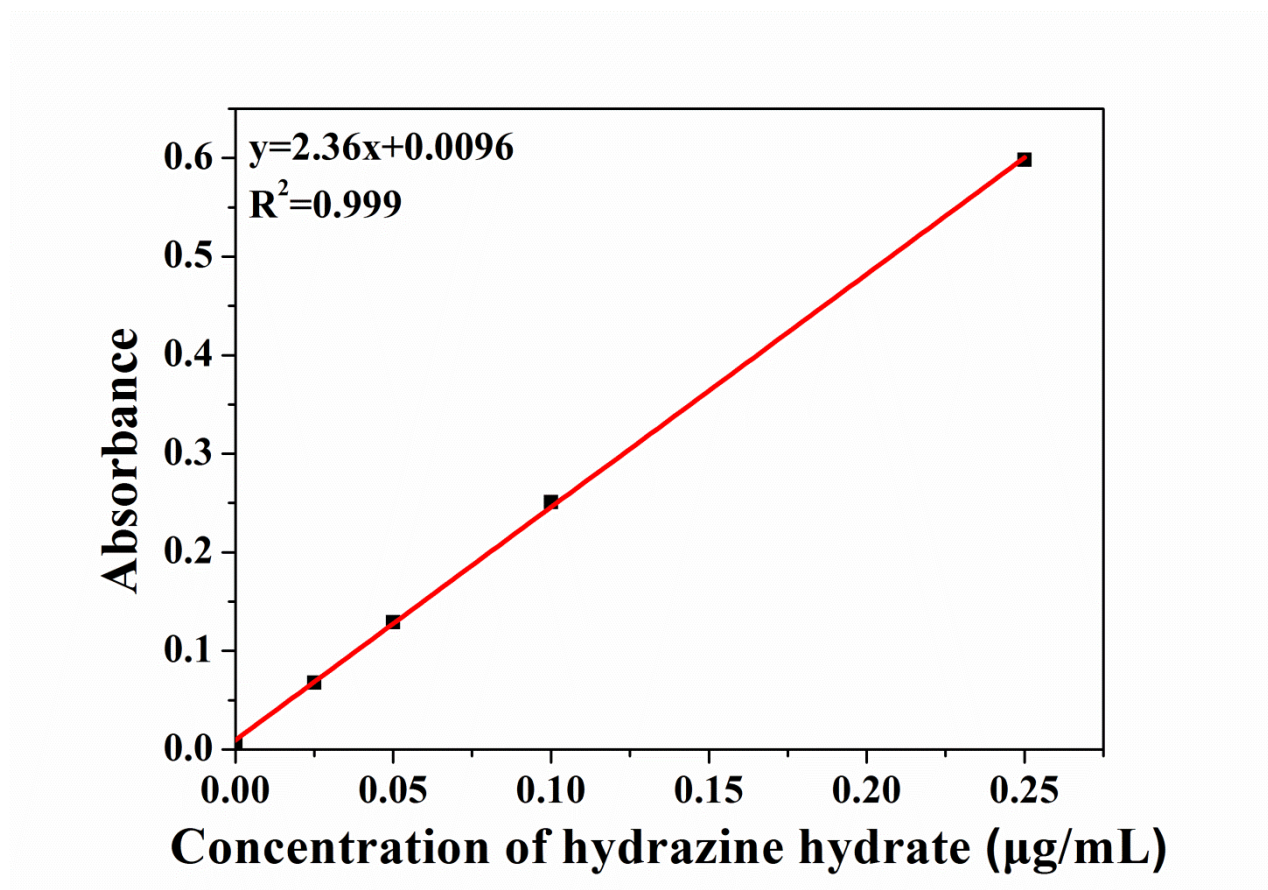


Figure S18 Calibration curve for the colorimetric $\text{N}_2\text{H}_4 \cdot \text{H}_2\text{O}$ assay using the method of Watt and Chrisp.

Table S2 The average yields and corresponding Faradaic efficiencies under various applied potentials.

E (vs. RHE)	Yield ($\mu\text{g h}^{-1} \text{ cm}^{-2} \text{ mg}_{\text{cat}}^{-1}$)		Total FE (%)
	FE (%)		
	NH ₃	N ₂ H ₄	
0.05	10.58 (19.1)	1.02 (1.4)	20.5
0.00	10.6 (22.6)	1.88 (3.7)	26.3
-0.05	10.14 (13.5)	1.77 (2.4)	15.9
-0.10	10.94 (11.29)	2.42 (2.2)	13.49
-0.15	11.92667 (8.35)	5.06 (3.6)	11.95
-0.20	12.25667 (5.53)	6.88 (3)	8.53
-0.25	13.86667 (3.13)	8.59 (1.8)	4.93
-0.30	14.20667 (2.16)	9.95 (1.4)	3.56

Table S3 A brief summary of the representative reports on electrochemical N₂ reduction in aqueous solutions at ambient conditions.

Temperature	Catalyst	Electrolyte	Yield	FE (%)	Potential	Ref.
25 °C	Au nanorod	0.1 M KOH	$1.648 \mu\text{g} \cdot \text{h}^{-1} \cdot \text{cm}^{-2}$	4.02	-0.2 V vs. RHE	[10]
25 °C	a-Au/CeO _x -RGO	0.1 M HCl	$8.3 \mu\text{g} \cdot \text{h}^{-1} \cdot \text{mg}^{-1}$	10.1	-0.2 V vs. RHE	[11]
R.T.	30 wt% Fe ₂ O ₃ -CNT	0.50 M KOH	$0.649 \mu\text{g} \cdot \text{h}^{-1} \cdot \text{cm}^{-2}$	0.164	-2.0 V vs Ag/AgCl	[12]
R.T.	VN Nanowires/CC	0.1 M HCl	$2.48 \times 10^{-10} \text{ mol s}^{-1} \text{ cm}^{-2}$	3.58	-0.3 V vs RHE	[13]
25 °C	ZIF-derived disordered carbon	0.1 M KOH	$9.22 \text{ mmol g}^{-1} \text{ h}^{-1}$	10.2	-0.3 V vs RHE	[14]
25 °C	B-doped graphene	0.05 M H ₂ SO ₄	$9.8 \mu\text{g cm}^{-2} \text{ h}^{-1}$	10.8	-0.5 V vs RHE	[15]
R.T.	Single Mo atoms anchored on N-doped porous carbon	0.1M KOH	$34.0 \text{ mg h}^{-1} \text{ mg}_{\text{cat}}^{-1}$	14.6	-0.3 V vs. RHE	[16]
R.T.	MoAlB SCs	0.1 M KOH	$9.2 \mu\text{g h}^{-1} \text{ cm}^{-2} \text{ mg}_{\text{cat}}^{-1}$	30.1	-0.05 V vs. RHE	[17]
R.T.	MIL-125 (Ti)-derived C-doped TiO ₂ /C	0.1 M LiClO ₄	$14.8 \text{ mg h}^{-1} \text{ mg}_{\text{cat}}^{-1}$	17.8	-0.4 V vs. RHE	[18]
R.T.	HKUST-1 (Cu-BTC)	0.1 M Na ₂ SO ₄	$4.66 \mu\text{g h}^{-1} \text{ cm}^{-2}$	2.45	-0.75 V vs. RHE	[19]
R.T.	MOF-derived C@NiO@Ni microtubes	0.1 M KOH	$43.15 \text{ mg h}^{-1} \text{ mg}_{\text{cat}}^{-1}$	10.9	-0.7 V vs. RHE	[20]
R.T.	PCN-222(Fe)-derived Fe ₁ -N-C	0.1 M HCl	$1.56 \times 10^{-11} \text{ mol cm}^{-2} \text{ s}^{-1}$	4.51	-0.05 V vs. RHE	[21]
R.T.	2D Co _x Fe-MOF	0.1 M KOH	$8.79 \text{ mg h}^{-1} \text{ mg}_{\text{cat}}^{-1}$	25.64	-0.2 V vs. RHE	[22]
R.T.	MIL-100 (AL)	0.1 M KOH	$10.6 \mu\text{g h}^{-1} \text{ cm}^{-2} \text{ mg}_{\text{cat}}^{-1}$	22.6	0.00 V vs. RHE	This work

References

- (1) Volkringer C.; Popov D.; Loiseau T.; Ferey G.; Burghammer M.; Riekel C.; Haouas M.; Taulelle F. Synthesis, Single-Crystal X-ray Microdiffraction, and NMR Characterizations of the Giant Pore Metal-Organic Framework Aluminum Trimesate MIL-100. *Chem. Mater.* **2009**, *21*, 5695–5697.
- (2) Cai J.-H.; Mao X.-H.; Song W.-G. Adsorption Behavior and Structure Transformation of Mesoporous Metal–Organic Frameworks towards Arsenates and Organic Pollutants in Aqueous Solution. *Mater. Chem. Front.* **2018**, *2*, 1389.
- (3) Shearer C.-G.; Chavan S.; Bordiga S.; Svelle S.; Olsbye U.; Lillerud P.-K. Defect Engineering: Tuning the Porosity and Composition of the Metal-Organic Framework UiO-66 via Modulated Synthesis. *Chem. Mater.* **2016**, *28*, 3749–3761.
- (4) Yang C.-X.; Ren H.-B.; Yan X.-P. Fluorescent Metal-Organic Framework MIL-53(Al) for Highly Selective and Sensitive Detection of Fe^{3+} in Aqueous Solution. *Anal. Chem.* **2013**, *85*, 7441–7446.
- (5) Biswas S.; Couck S.; Denysenko D.; Bhunia A.; Grzywa M.; Denayer F.-M.-J.; Volkmer D.; Janiak C.; Voort D.-V.-P. Sorption and Breathing Properties of Difluorinated MIL-47 and Al-MIL-53 Frameworks. *Micropor. Mesopor. Mat.* **2013**, *181*, 175–181.
- (6) Wang J. ; Yu L. ; Hu L. ; Chen G. ; Xin H.-L. ; Feng X.-F. Ambient Ammonia Synthesis via Palladiumcatalyzed Electrohydrogenation of Dinitrogen at Low Overpotential. *Nat. Commun.* **2018**, *9*, 1795.
- (7) Rumble J. CRC Handbook of Chemistry and Physics 98th Edition. *CRC Press*, Boca Raton, Florida, **2017**.

- (8) Cui Q.-Y.; Qin G.-Q.; Wang W.-H.; Geethalakshmi K.-R.; Du A.-J.; Sun Q. Mo-based 2D MOF as a Highly Efficient Electrocatalyst for Reduction of N₂ to NH₃: A Density Functional Theory Study. *J. Mater. Chem. A* **2019**, *7*, 14510.
- (9) Watt G.-W.; Chrisp J.-D. Spectrophotometric Method for the Determination of Hydrazine. *Anal. Chem.* **1952**, *24*, 2006–2008.
- (10) Bao D.; Zhang Q.; Meng F.-L.; Zhong H.-X.; Shi M.-M.; Zhang Y.; Yan J.-M.; Jiang Q.; Zhang X.-B. Electrochemical Reduction of N₂ under Ambient Conditions for Artificial N₂ Fixation and Renewable Energy Storage using N₂/NH₃ Cycle. *Adv. Mater.* **2017**, *29*, 1604799.
- (11) Li S.-J.; Bao D.; Shi M.-M.; Wulan B.-R.; Yan J.-M.; Jiang Q. Amorphizing of Au Nanoparticles by CeO_x-RGO Hybrid Support towards Highly Efficient Electrocatalyst for N₂ Reduction under Ambient Conditions. *Adv. Mater.* **2017**, *29*, 1700001.
- (12) Chen S.; Perathoner S.; Ampelli C.; Mebrahtu C.; Su D.; Centi G. Room-Temperature Electrocatalytic Synthesis of NH₃ from H₂O and N₂ in a Gas–Liquid–Solid Three-Phase Reactor. *ACS Sustainable Chem. Eng.* **2017**, *5*, 7393.
- (13) Zhang X.; Kong R.; Du H.; Xia L.; Qu F. Highly Efficient Electrochemical Ammonia Synthesis via Nitrogen Reduction Reactions on a VN Nanowire Array under Ambient Conditions. *Chem. Commun.* **2018**, *54*, 5323–5325.
- (14) Mukherjee S.; Cullenb D.-A.; Karakalosc S.; Liud K.; Zhanga H.; Zhaoe S.; Xue H.; More K.-L.; Wang G.; Wu G. Metal-Organic Framework-Derived Nitrogen-Doped Highly Disordered Carbon for Electrochemical Ammonia Synthesis using N₂ and H₂O in Alkaline Electrolytes. *Nano Energy* **2018**, *48*, 217.
- (15) Yu X.; Han P.; Wei Z.; Huang L.; Gu Z.; Peng S.; Ma J.; Zheng G. Boron-Doped Graphene for Electrocatalytic N₂ Reduction. *Joule* **2018**, *2*, 1610.

- (16) Han L.-L.; Liu X.-J.; Chen J.-P.; Lin R.-Q.; Liu H.-X.; Lu F.; Bak S.; Liang Z.-X.; Zhao S.-Z., Stavitski E.; Luo J.; Adzic R.-R., Xin H.-L. Atomically Dispersed Molybdenum Catalysts for Efficient Ambient Nitrogen Fixation. *Angew. Chem. Int. Ed.* **2019**, *58*, 2321–2325.
- (17) Fu Y.; Richardson P.; Li K.-K.; Yu H.; Yu B.; Donne S.; Kisi E.; Ma T.-Y. Transition Metal Aluminum Boride as a New Candidate for Ambient-Condition Electrochemical Ammonia Synthesis. *Nano-Micro Lett.* **2020**, *12*, 65.
- (18) Qin Q.; Zhao Y.; Schmallegger M.; Heil T.; Schmidt J.; Walczak R.; Gescheidt-Demner G.; Jiao H.-J.; Oschatz M. Enhanced Electrocatalytic N₂ Reduction via Partial Anion Substitution in Titanium Oxide–Carbon Composites. *Angew. Chem. Int. Ed.* **2019**, *58*, 13101–13106.
- (19) Cao Y.-M.; Li P.-P.; Wu T.-T.; Liu M.-L.; Zhang Y.-Y. Electrocatalysis of N₂ to NH₃ by HKUST-1 with High NH₃ Yield. *Chem Asian J.* **2020**, *15*, 1272–1276.
- (20) Luo S.-J.; Li X.-M.; Gao W.-G.; Zhang H.-Q.; Luo M. An MOF-Derived C@NiO@Ni Electrocatalyst for N₂ Conversion to NH₃ in Alkaline Electrolytes. *Sustain. Energy Fuels* **2020**, *4*, 164.
- (21) Zhang R.; Jiao L.; Yang W.-J.; Wan G.; Jiang H.-L. Single-Atom Catalysts Templated by Metal-Organic Frameworks for Electrochemical Nitrogen Reduction. *J. Mater. Chem. A* **2019**, *7*, 26371–26377.
- (22) Li W.-X.; Fang W.; Wu C.; Dinh K.-N.; Ren Hao.; Zhao L. Liu C.-T.; Yan Q.-Y. Bimetal-MOF Nanosheets as Efficient Bifunctional Electrocatalysts for Oxygen Evolution and Nitrogen Reduction Reaction. *J. Mater. Chem. A* **2020**, *8*, 3658.